AIP | Physics of Plasmas

Synergy between ion temperature gradient turbulence and neoclassical processes in global gyrokinetic particle-in-cell simulations

T. Vernay, S. Brunner, L. Villard, B. F. McMillan, S. Jolliet et al.

Citation: Phys. Plasmas **19**, 042301 (2012); doi: 10.1063/1.3699189
View online: http://dx.doi.org/10.1063/1.3699189
View Table of Contents: http://pop.aip.org/resource/1/PHPAEN/v19/i4
Published by the American Institute of Physics.

Related Articles

Second harmonic electromagnetic emission of a turbulent magnetized plasma driven by a powerful electron beam
Phys. Plasmas 19, 044501 (2012)

Dissipation range turbulent cascades in plasmas
Phys. Plasmas 19, 055906 (2012)

Thermal plasma and fast ion transport in electrostatic turbulence in the large plasma device
Phys. Plasmas 19, 055904 (2012)

Impact of resonant magnetic perturbations on nonlinearly driven modes in drift-wave turbulence
Phys. Plasmas 19, 055903 (2012)

Evidence of critical balance in kinetic Alfvén wave turbulence simulations

Phys. Plasmas 19, 055901 (2012)

Additional information on Phys. Plasmas

Journal Homepage: http://pop.aip.org/
Journal Information: http://pop.aip.org/about/about_the_journal
Top downloads: http://pop.aip.org/features/most_downloaded
Information for Authors: http://pop.aip.org/authors

ADVERTISEMENT

Downloaded 12 Apr 2012 to 128.178.234.18. Redistribution subject to AIP license or copyright; see http://pop.aip.org/about/rights_and_permissions

Synergy between ion temperature gradient turbulence and neoclassical processes in global gyrokinetic particle-in-cell simulations

T. Vernay,[1] S. Brunner,[1] L. Villard,[1] B. F. McMillan,[2] S. Jolliet,[1] T. M. Tran,[1] and A. Bottino[3]
[1]*Centre de Recherches en Physique des Plasmas, Ecole Polytechnique Fédérale de Lausanne (EPFL), Association EURATOM – Confédération Suisse, CH-1015 Lausanne, Switzerland*
[2]*Centre for Fusion, Space and Astrophysics, Department of Physics, University of Warwick, Coventry CV4 7AL, United Kingdom*
[3]*Max-Planck-Institut für Plasmaphysik, Boltzmannstrasse 2, EURATOM Association, D-85748 Garching, Germany*

(Received 3 November 2011; accepted 14 March 2012; published online 5 April 2012)

Based on the CYCLONE case, simulations of collisional electrostatic ion temperature gradient (ITG) microturbulence carried out with the global gyrokinetic particle-in-cell (PIC) code ORB5 are presented. Considering adiabatic electrons, an increase in ion heat transport over the collisionless turbulent case due to ion-ion collisions is found to exceed the neoclassical contribution. This synergetic effect is due to interaction of collisions, turbulence, and zonal flows. When going from a collisionless to a collisional ITG turbulence simulation, a moderate reduction of the average zonal flow level is observed. The collisional zonal flow level turns out to be roughly independent of the finite collisionality considered. The Dimits shift softening by collisions [Z. Lin *et al.*, Phys. Rev. Lett. **83**, 3645 (1999)] is further characterized, and the shearing rate saturation mechanism is emphasized. Turbulence simulations start from a neoclassical equilibrium [T. Vernay *et al.*, Phys. Plasmas **17**, 122301 (2010)] and are carried out over significant turbulence times and several collision times thanks to a coarse-graining procedure, ensuring a sufficient signal/noise ratio even at late times in the simulation. The relevance of the Lorentz approximation for ion-ion collisions, compared to a linearized Landau self-collision operator, is finally addressed in the frame of both neoclassical and turbulence studies. [http://dx.doi.org/10.1063/1.3699189]

I. INTRODUCTION

The effect of the radial electric field related to axisymmetric modes and the associated zonal flows on tokamak microturbulence has been widely studied in the frame of gyrokinetic simulations. In particular, the ion temperature gradient (ITG) turbulence saturation due to vortice shearing produced by zonal flows is a well established mechanism, which reduces the turbulent transport in ITG-dominated regimes.[1–4] Due to the high temperatures in the core of tokamak plasmas, collisionless gyrokinetic models have extensively been used for turbulent transport analysis. However, even though collisionality is not *a priori* a dominant effect for the core tokamak physics, it may nonetheless significantly affect the transport in at least three ways. First, collisions produce an intrinsical neoclassical transport. Usually small compared to the turbulent transport, neoclassical transport may nevertheless reach comparable levels, in conditions of marginal stability of microinstabilities. Second, collisions *damp* radial perturbations and associated zonal flows as predicted in Ref. 5. Third, collisions may, in fact, also *generate* a neoclassical radial electric field for ensuring ambipolarity in the presence of density and temperature gradients, leading to background $\vec{E} \times \vec{B}$ flows. This strong effect of collisions on radial electric field dynamics, appearing through a competition between generation and damping, affects in turn through zonal flow shearing the turbulent transport levels, as studied in this paper.

In order to address issues related to collisional turbulent transport with a particle-in-cell (PIC) code, such as ORB5,[6,7] the first requirement is to ensure long and relevant simulations despite the numerical noise intrinsic to the PIC method and even enhanced over time by the numerical treatment of collisions. The code ORB5 has proven to enable long, statistically converged collisionless simulations by using a small artificial decay of the weights.[8] The latter noise control scheme is, however, unpractical for carrying out collisional simulations, since the required numerical decay rate which needs to be chosen for the approach to be effective is typically of the order of the ion-ion collision frequency and may thus significantly interfere with the corresponding physical effects. The control of numerical noise in presence of collisions is thus handled by making use of the so-called coarse-graining procedure, first proposed in Ref. 9 and further simplified in Ref. 10. Some details related to the implementation of the coarse-graining algorithm in ORB5 had already been given in Ref. 11 for carrying out neoclassical simulations. The generalization of this implementation in ORB5 for handling turbulence simulations is described in this paper.

Another requirement for the code is to feature a robust and thoroughly tested collision operator. The self-collision operators in ORB5 are linearized Landau operators conserving locally the first three velocity moments (density, parallel momentum, and kinetic energy) and whose discretization is presented in detail in Ref. 11. Several neoclassical benchmarks against other codes and analytical predictions have

Downloaded 12 Apr 2012 to 128.178.234.18. Redistribution subject to AIP license or copyright; see http://pop.aip.org/about/rights_and_permissions

been performed. In this paper, we also address the question of whether a simple Lorentz operator for ion-ion collisions used in other codes[12] is sufficient for turbulence studies compared to a more accurate Landau self-collision operator.

Studies of collisional ITG turbulence using gyrokinetic simulations have already been performed in the past, making use of Lagrangian (PIC),[13] Semi-Lagrangian,[14] and Eulerian[15] methods. In Ref. 13, the damping of zonal flows by collisions is found to increase the turbulent heat diffusivity, at all values of the gradients considered. An Eulerian approach combined with a simplified Krook operator for ion-ion collisions provides the same trend, however, somewhat less pronounced.[16] Turbulence studies in the frame of a Z-pinch configuration show as well a transport enhancement due to collisions.[17] This general conclusion is confirmed by ORB5 results. In this paper, we systematically analyze the mechanisms of neoclassical (purely collisional) and turbulent transport, as well as their possible interactions. To this end, in a first phase of the simulation, a neoclassical equilibrium is established by keeping only axisymmetric ($n=0$) Fourier modes. In a second phase, turbulence can evolve freely by considering all toroidal Fourier modes ($n=0$ and $n\neq 0$). Our simulations show that collisional effects are not simply additive to collisionless turbulent transport: heat transport in the presence of both turbulence and collisions is larger than the sum of collisionless turbulent transport and neoclassical transport. The softening of the Dimits shift region obtained in Ref. 13 is as well observed in ORB5 simulations and is further characterized in this work. However, the bursting behaviour of the zonal flows in the Dimits shift region predicted in Ref. 13 is only clearly reproduced for narrow gradient profiles. For wider gradient profiles, a steadier regime is observed. Additional drive from increased turbulence levels in collisional simulations is found to essentially balance the zonal flow damping by collisions, leading to zonal flow amplitudes only slightly reduced in collisional simulations compared to the collisionless situation. Moreover, the zonal flow levels in collisional simulations turn out to be roughly independent of the finite collisionality considered. The zonal flow saturation, due to a tertiary instability mechanism transferring energy from zonal modes back to turbulence and occurring at large ion temperature gradients, is demonstrated.[18] Like the previous results mentioned above, the electrons are assumed adiabatic and therefore collisionless in this paper. Considering the dynamics of kinetic electrons along with the related electron collisionality may lead to different conclusions concerning the effects of collisions on turbulence in certain regimes,[19] mainly due to the reduction of microinstability drive by electron collisions.

The paper is organized as follows: Sec. II presents briefly the simulation model and the numerical method, as well as the parameters of the specific considered physical system. Section III explains the noise control procedure applied in collisional ORB5 and shows some related tests. Section IV presents some results related to collisional Rosenbluth-Hinton (RH) tests, which emphasize the difference in poloidal $\vec{E}\times\vec{B}$ flow physics between collisionless and collisional systems. Section V shows how ORB5 collisional simulations of turbulence are started from a neoclassical equilibrium. It addresses the synergetic effect of collisions on the total transport for different temperature gradients and demonstrates the zonal flow saturation mechanism through tertiary instabilities. Section VI considers the relevance of the simple Lorentz operator for ion-ion collisions in the frame of turbulence studies. Conclusions are drawn in Sec. VII.

II. SIMULATION MODEL AND NUMERICAL METHODS

A. The gyrokinetic equation

Simulations are performed with the global gyrokinetic code ORB5.[6,7] Electrons are considered here in the limit of the adiabatic approximation as one is interested in the purely ITG regime. The collisional model of ORB5 is described in detail in Ref. 11. It solves the gyrokinetic equation for the gyro-averaged ion distribution function $f(\vec{R},v_{||},\mu,t)$, where $\vec{R}$ is the gyrocenter position, $v_{||}$ is the parallel velocity, and $\mu=mv_{\perp}^2/2B$ is the magnetic moment. The operator $\hat{C}$ representing ion-ion collisions is a Landau operator, which does not retain the Finite-Larmor-Radius effects, linearized with respect to a non-shifted local Maxwellian distribution f_{LM}:

$$\hat{C}(\delta f_{LM}) = C[f_{LM},\delta f_{LM}] + C[\delta f_{LM},f_{LM}], \tag{1}$$

where $\delta f_{LM}=f-f_{LM}$ represents the deviation of the full distribution f with respect to f_{LM}. The first term on the right hand side represents collisions of δf_{LM} on the background f_{LM} and the second term represents the background reaction (collisions of f_{LM} on δf_{LM}) ensuring the local conservation of density, parallel momentum, and kinetic energy. The background reaction term is in fact approximated and of the form:[9,20]

$$\frac{C[\delta f_{LM},f_{LM}]}{f_{LM}} \simeq \mathcal{B}(\delta f_{LM}) = \frac{1}{n_0}\left\{6\sqrt{\pi}H(\mathsf{v})\frac{\delta\mathcal{P}_{||}v_{||}}{v_{th}^2}+\sqrt{\pi}G(\mathsf{v})\frac{\delta\mathcal{E}}{v_{th}^2}\right\}, \tag{2}$$

where n_0 is the background density, $v_{th}=\sqrt{T/m}$ is the thermal velocity, and $\mathsf{v}=v/v_{th}$. $H(\mathsf{v})$ and $G(\mathsf{v})$ are defined in Ref. 11 and related to the Rosenbluth potentials relatively to a Maxwellian background. $\delta\mathcal{P}_{||}$ and $\delta\mathcal{E}$ are, respectively, the changes in the parallel momentum and the kinetic energy of the fluctuation distribution due to $C[f_{LM},\delta f_{LM}]$:

$$\delta\mathcal{P}_{||}(\delta f_{LM},\vec{R}) = -\int C[f_{LM},\delta f_{LM}]v_{||}\mathrm{d}^3v, \tag{3}$$

$$\delta\mathcal{E}(\delta f_{LM},\vec{R}) = -\int C[f_{LM},\delta f_{LM}]v^2\mathrm{d}^3v. \tag{4}$$

The form (2) ensures the same symmetry properties as the exact background reaction term and associated properties (H-theorem, stationary states). A heat source S_H is also considered, such that the gyrokinetic equation reads:

$$\frac{D}{Dt}f = -\hat{C}(\delta f_{LM}) + S_H, \tag{5}$$

Downloaded 12 Apr 2012 to 128.178.234.18. Redistribution subject to AIP license or copyright; see http://pop.aip.org/about/rights_and_permissions

where D/Dt is the collisionless gyrokinetic operator:

$$\frac{D}{Dt} = \frac{\partial}{\partial t} + \frac{\mathrm{d}\vec{R}}{\mathrm{d}t} \cdot \frac{\partial}{\partial \vec{R}} + \frac{\mathrm{d}v_{||}}{\mathrm{d}t} \frac{\partial}{\partial v_{||}}. \tag{6}$$

The gyrokinetic equations of motion for the gyrocenter variables, derived by Hahm,[21] are given by:

$$\frac{\mathrm{d}\vec{R}}{\mathrm{d}t} = \vec{v}_G = v_{||}\hat{b} + \underbrace{\vec{v}_{\nabla B} + \vec{v}_c + \vec{v}_{E\times B}}_{\vec{v}_d}, \tag{7}$$

$$\frac{\mathrm{d}v_{||}}{\mathrm{d}t} = \frac{1}{mv_{||}} \vec{v}_G \cdot (q\vec{E} - \mu\vec{\nabla}B), \tag{8}$$

$$\frac{\mathrm{d}\mu}{\mathrm{d}t} = 0, \tag{9}$$

which are valid for small fluctuation levels. Here, $\hat{b} = \vec{B}/B$ is the unitary vector along $\vec{B}$, $\vec{v}_G$ is the guiding center velocity, $\vec{v}_{\nabla B}$ is the ∇B drift velocity, $\vec{v}_c$ is the curvature drift velocity, $\vec{v}_{E\times B}$ is the $\vec{E}\times\vec{B}$ drift velocity, and $\vec{E}$ is the gyro-averaged electric field deriving from the electrostatic potential ϕ. For more details, the reader is referred to Ref. 7.

B. δf Particle-in-cell discretization

ORB5 uses the low noise δf PIC method, requiring the introduction of N numerical particles, called markers, for sampling the fluctuation distribution δf. The distribution f is split into a background distribution f_0 and a perturbed part $\delta f = f - f_0$. Introducing two weights $w_r(t)$ and $p_r(t)$ for the marker r, the fluctuation distribution δf and associated background distribution f_0, respectively, read:

$$\delta f(\vec{R}, v_{||}, \mu, t) = \sum_{r=1}^{N} \frac{m}{B_{||}^*} w_r(t) \delta[\vec{R} - \vec{R}_r(t)] \delta[v_{||} - v_{||,r}(t)] \times \delta[\mu - \mu_r(t)], \tag{10}$$

$$f_0(\vec{R}, v_{||}, \mu) = \sum_{r=1}^{N} \frac{m}{B_{||}^*} p_r(t) \delta[\vec{R} - \vec{R}_r(t)] \delta[v_{||} - v_{||,r}(t)] \times \delta[\mu - \mu_r(t)], \tag{11}$$

where $B_{||}^* = B + mv_{||}(\vec{\nabla}\times\hat{b})\cdot\hat{b}/q$ and r is an indice for labelling the N markers. δ stands here for the Dirac function. The gyrokinetic equation is solved through a time splitting approach, considering successively and separately the time stepping of the collisionless dynamics, the collisional dynamics, and the source term S_H.

1. Collisionless stepping

For solving the collisionless part of the dynamics, the background f_0 is chosen as a so-called canonical Maxwellian $f_{CM}(\hat{\Psi}, \mathcal{E})$:[22]

$$f_{CM}(\hat{\Psi}, \mathcal{E}) = \frac{n_0(\hat{\Psi})}{[2\pi T_0(\hat{\Psi})/m]^{3/2}} \exp\left[-\frac{\mathcal{E}}{T_0(\hat{\Psi})}\right], \tag{12}$$

where the radial coordinate $\hat{\Psi}$ is the corrected toroidal canonical momentum and reads:

$$\hat{\Psi} = \Psi_0 + \mathrm{corr} = \Psi_0 - \mathrm{sign}(v_{||})\frac{m}{q}R_0\sqrt{\frac{2}{m}(\mathcal{E} - \mu B_0)}\mathcal{H}(\mathcal{E} - \mu B_0), \tag{13}$$

with $\mathcal{H}$ the Heaviside function, $\mathcal{E} = mv^2/2 = mv_{||}^2/2 + \mu B$ the kinetic energy, and B_0 the magnetic field at the magnetic axis. The correction in $\hat{\Psi}$ to the toroidal canonical momentum $\Psi_0 = \Psi + mF(\Psi)v_{||}/qB$, where $F(\Psi) = RB_\varphi$, is set to zero for trapped particles and of opposite sign for forward and backward passing particles. $\hat{\Psi}$, being clearly a function of constants of the unperturbed motion, is itself a constant of motion of the unperturbed system. f_{CM} is thus a function of the constants of the unperturbed motion, $(\hat{\Psi}, \mathcal{E}, \mu)$, and is therefore solution of the stationary, collisionless gyrokinetic equation in absence of perturbations. Since the constant of motion $\hat{\Psi}$ of a given particle provides a good estimate of the average $\langle\Psi\rangle_{\mathrm{traj}}$ of the magnetic flux coordinate Ψ over the guiding center trajectory,[22] the profiles $n_0(\Psi)$ and $T_0(\Psi)$ are close to the effective density and temperature profiles of the background $f_{CM}(\hat{\Psi})$. Moreover, note that choosing the background f_{CM} as a function of the corrected toroidal canonical momentum $\hat{\Psi}$ has the purpose of defining an equilibrium with essentially zero toroidal rotation.[23]

Evolving the collisionless part of the gyrokinetic equation is thus performed by integrating numerically in time Eqs. (7)–(9) to obtain the collisionless marker trajectories $z_r(t) = [\vec{R}_r(t), v_{||,r}(t), \mu_r(t)]$ together with weight equations $\mathrm{d}w_r/\mathrm{d}t$ and $\mathrm{d}p_r/\mathrm{d}t$, detailed in Ref. 11 and written as follows:

$$\frac{\mathrm{d}}{\mathrm{d}t} w_r(t) = -p_r(t) \frac{1}{f_{CM}} \frac{D}{Dt} f_{CM}\Big|_{[z_r(t),t]}, \tag{14}$$

$$\frac{\mathrm{d}}{\mathrm{d}t} p_r(t) = p_r(t) \frac{1}{f_{CM}} \frac{D}{Dt} f_{CM}\Big|_{[z_r(t),t]}. \tag{15}$$

The collisionless dynamics is handled through the so-called direct-δf method,[24] taking advantage of the fact that the total distribution f is conserved along collisionless trajectories. The weight equations for collisionless dynamics can in fact be integrated analytically:

$$\frac{\mathrm{d}}{\mathrm{d}t}(w_r(t) + p_r(t)) = 0 \Rightarrow w_r + p_r = \mathrm{const.}, \tag{16}$$

$$\frac{\mathrm{d}}{\mathrm{d}t} \ln \frac{p_r}{f_{CM}|_{z_r}} = 0 \Rightarrow \frac{p_r}{f_{CM}|_{z_r}} = \mathrm{const.}; \tag{17}$$

Equation (16) resulting from adding relations (14) and (15) and Eq. (17) obtained directly from integration of Eq. (15). Let us suppose a marker r going from position $z_r(t) = [\vec{R}_r(t), v_{||,r}(t), \mu_r(t)]$ to position $z_r(t+\Delta t) = [\vec{R}_r(t+\Delta t), v_{||,r}(t+\Delta t), \mu_r(t+\Delta t)]$ during a collisionless time step $t \to t + \Delta t$. Making use of Eqs. (16) and (17), the new weights are given by:

Downloaded 12 Apr 2012 to 128.178.234.18. Redistribution subject to AIP license or copyright; see http://pop.aip.org/about/rights_and_permissions

$$p_r(t+\Delta t) = p_r(t)\frac{f_{CM}|_{z_r(t+\Delta t)}}{f_{CM}|_{z_r(t)}}, \tag{18}$$

$$w_r(t+\Delta t) = w_r(t) + p_r(t) - p_r(t+\Delta t). \tag{19}$$

This scheme allows to avoid evaluating explicitly unpractical terms, such as $\mathrm{d}\hat{\Psi}/\mathrm{d}t$, appearing through Df_{CM}/Dt in Eqs. (14) and (15) for the time evolution of the weights.

2. Collisional stepping

For the purely collisional part of the time splitting approach, the background f_0 is chosen as a local Maxwellian $f_{LM}(\Psi,\mathcal{E})$:

$$f_{LM}(\Psi,\mathcal{E}) = \frac{n_0(\Psi)}{[2\pi T_0(\Psi)/m]^{3/2}}\exp\left[-\frac{\mathcal{E}}{T_0(\Psi)}\right], \tag{20}$$

where Ψ is the poloidal magnetic flux and $n_0(\Psi)$ and $T_0(\Psi)$ are the background density and temperature profiles, respectively. The transition between the local background f_{LM} representation and the canonical background f_{CM} representation, used for solving the collisional and the collisionless dynamics, respectively, is provided by the background switching scheme described in detail in Ref. 11. Collisions of δf_{LM} on f_{LM}, so-called test particle collisions represented by $C[f_{LM},\delta f_{LM}]$, are modelled through random kicks for markers in velocity space, according to the Langevin approach, while collisions of f_{LM} on δf_{LM} appear through the following collisional weight equations:

$$\frac{\mathrm{d}}{\mathrm{d}t}w_r(t) = -p_r(t)\frac{C[\delta f_{LM},f_{LM}]}{f_{LM}}\bigg|_{[z_r(t),t]}, \tag{21}$$

$$\frac{\mathrm{d}}{\mathrm{d}t}p_r(t) = 0. \tag{22}$$

The background reaction implementation ensures the conservation of density, parallel momentum, and kinetic energy to round-off precision through the numerical computation of the fields (3) and (4).[25] The challenge of evolving the marker weights in the collisional step reduces to the accurate estimates of $\delta\mathcal{P}_{||}(\vec{R},t)$ and $\delta\mathcal{E}(\vec{R},t)$ representing the local variations in time of parallel momentum and kinetic energy resulting from test particle collisions and appearing in the background reaction $C[\delta f_{LM},f_{LM}]$ of the linearized collision operator as shown in Eq. (2). In practice, $\delta\mathcal{P}_{||}$ and $\delta\mathcal{E}$ are estimated by a binning procedure. More details about the numerical methods are given in Ref. 11. Note, however, that for the axisymmetric neoclassical runs described in Ref. 11, only a two-dimensional binning of markers in the poloidal plane (bins with respect to a (Ψ,θ^*) grid) needed to be considered for estimating the fields $\delta\mathcal{P}_{||}$ and $\delta\mathcal{E}$, while for the here considered turbulence runs, a three-dimensional binning needs to be considered as the turbulence structures vary along all configuration space dimensions. The binning related to collisions is field-aligned, in order to take advantage of the turbulence structure, and equivalent to the binning for the coarse-graining in configuration space described in Sec. III.

The collisionality is defined through the normalized ν^* parameter, which is the ratio between the detrapping collision frequency and the bounce frequency:

$$\nu^* = \frac{R_0 q_s}{\tau_{ii} v_{thi}\epsilon^{3/2}}, \quad \text{with} \quad \tau_{ii} = \frac{6\sqrt{\pi}}{\nu_{ii}}, \tag{23}$$

where ν_{ii} is the thermal self-collision frequency for ions:

$$\nu_{ii} = \frac{n_i q_i^4 \ln\Lambda}{2\pi\epsilon_0^2 m_i^2 v_{thi}^3}. \tag{24}$$

The Coulomb logarithm $\ln\Lambda$ is assumed to be constant over the whole plasma and typically chosen $\ln\Lambda = 18$. Except for the Coulomb logarithm, the radial dependence of the collisionality, through density and temperature profiles, is accounted for. The notation ν_0^* is introduced and stands for the collisionality parameter at a reference surface.

3. Heat sources

The heat source brings an additional term to the gyrokinetic equation (5) in order to maintain an effective ion temperature profile $T = T(\Psi)$. Transport processes thus tend to relax the temperature profile, while source terms tend to readjust it towards the reference background profile. The effective time-averaged profile thus equilibrates more or less near the reference background profile depending on the strength of the relaxation parameter γ_H in the source term (see Eq. (25)). The use of the heat source in global ORB5 simulations thus allows to study gradient-driven turbulence in a quasi-stationary state. In a simulation with no heat sources, temperature gradients relax too quickly, especially in small systems (low $1/\rho^*$ values), and turbulent transport thus remains in a transient regime, which is inappropriate for studying quasi-stationary turbulence. The heat source takes the form (for more details see Ref. 8):

$$S_H = -\gamma_H\left(\widetilde{\delta f}_{CM}(\Psi,\mathcal{E},t) - \widetilde{f_{CM}}(\Psi,\mathcal{E},t)\frac{\int \mathrm{d}\mathcal{E}\widetilde{\delta f}_{CM}(\Psi,\mathcal{E},t)}{\int \mathrm{d}\mathcal{E}\widetilde{f_{CM}}(\Psi,\mathcal{E},t)}\right), \tag{25}$$

where the symbol $\tilde{}$ stands for the operator which reconstructs the distribution in the $(\Psi,\mathcal{E})$ space. For any function A of the gyrocenter variables $(\Psi,\theta^*,\varphi,\mathcal{E},\xi)$, where θ^* is the straight-field-line poloidal angle, φ is the toroidal angle, and $\xi = v_{||}/v$ is the pitch angle, this operator reads:

$$\tilde{A}(\Psi,\mathcal{E},t) = \frac{\int \mathrm{d}\theta^*\mathrm{d}\varphi\mathrm{d}\xi(B_{||}^*/B)J_{\Psi\theta^*\varphi}A(\Psi,\theta^*,\varphi,\mathcal{E},\xi,t)}{\int \mathrm{d}\theta^*\mathrm{d}\varphi\mathrm{d}\xi J_{\Psi\theta^*\varphi}}, \tag{26}$$

$J_{\Psi\theta^*\varphi}$ being the Jacobian related to the (Ψ,θ^*,φ) coordinates. The heating rate γ_H is typically chosen as 10% of the linear growth rate of the most unstable ITG mode. The second term on the right hand side of Eq. (25) ensures that the source is particle conserving, i.e., no density perturbation is introduced. This heat source is also momentum conserving, as S_H is independent of sign$(v_{||})$, and therefore in particular

Downloaded 12 Apr 2012 to 128.178.234.18. Redistribution subject to AIP license or copyright; see http://pop.aip.org/about/rights_and_permissions

does not affect the long-wavelength zonal flows, which is a crucial requirement for relevant ITG turbulence simulations as discussed in detail in Ref. 8. Equation (25) is integrated separately from other dynamics in the frame of the time splitting approach.

C. Quasi-neutrality equation

The electrostatic approximation is assumed in our model. The electrons are considered adiabatic and enter the model through the quasi-neutrality equation:

$$\frac{en_{i0}(\Psi)}{T_e(\Psi)}[\phi(\vec{x},t)-\langle\phi\rangle(\Psi,t)]-\nabla_\perp\cdot\left(\frac{n_{i0}(\Psi)}{B\Omega_i}\nabla_\perp\phi\right)=\overline{\delta n_i}(\vec{x},t), \tag{27}$$

where ϕ is the electrostatic potential, $T_e(\Psi)$ is the electron temperature profile, Ω_i is the ion cyclotron frequency, e is the elementary charge, and $\langle\rangle$ stands for the flux-surface-average operator. $\overline{\delta n_i}(\vec{x},t)$ is the perturbed ion gyrodensity, computed as follows:

$$\overline{\delta n_i}(\vec{x},t)=\int\frac{B_\parallel^*}{m}\mathrm{d}^3R\,\mathrm{d}v_\parallel\,\mathrm{d}\mu\,\mathrm{d}\alpha_g\,\delta f_{CM,i}(\vec{R},v_\parallel,\mu,t)\times\delta(\vec{R}+\vec{\rho}_{Li}-\vec{x}), \tag{28}$$

where $\delta f_{CM,i}=f_i-f_{CM,i},\alpha_g$ is the gyroangle and $\vec{\rho}_{Li}(\mu,\alpha_g)$ is the ion Larmor vector. It is assumed that the ion background gyrodensity, defined as:

$$\bar{n}_{i0}(\vec{x})=\int\frac{B_\parallel^*}{m}\mathrm{d}^3R\,\mathrm{d}v_\parallel\,\mathrm{d}\mu\,\mathrm{d}\alpha_g f_{CM,i}(\vec{R},v_\parallel,\mu)\delta(\vec{R}+\vec{\rho}_{Li}-\vec{x}), \tag{29}$$

is equal to the ion background density $n_{i0}(\hat{\Psi})$ associated to the background distribution $f_{CM,i}$. One assumes, furthermore, that the background densities of electrons and ions verify quasi-neutrality, i.e., $Zn_{i0}=n_{e0}$, where Z is the ion charge. The last term on the left hand side of Eq. (27) is the linearized polarization drift, derived considering the long wavelength approximation ($k_\perp\rho_{Li}\ll 1$, where ρ_{Li} is the ion Larmor radius). Under this assumption, the polarization drift term, which, in general, is an integral operator, reduces to a differential operator (Poisson-like equation) and is valid only up to second order in $k_\perp\rho_{Li}$. Note that the considered adiabatic electron response is also linearized, having furthermore invoked small amplitude fluctuations, so that $|e(\phi-\langle\phi\rangle)/T_e|\ll 1$. The details of the numerical implementation of the quasi-neutrality equation solver are given in Refs. 7 and 26.

D. Transport diagnostics

We define, respectively, the gyrocenter particle flux Γ, the kinetic energy flux Q_{kin}, the potential energy flux Q_{pot}, and the heat flux q_H as follows:

$$\Gamma=\left\langle\frac{\vec{\nabla}\Psi}{|\vec{\nabla}\Psi|}\cdot\int\mathrm{d}^3v\,f\frac{\mathrm{d}\vec{R}}{\mathrm{d}t}\right\rangle=\left\langle\frac{1}{|\vec{\nabla}\Psi|}\int\mathrm{d}^3v\,f\frac{\mathrm{d}\Psi}{\mathrm{d}t}\right\rangle, \tag{30}$$

$$Q_{\mathrm{kin}}=\left\langle\frac{1}{|\vec{\nabla}\Psi|}\int\mathrm{d}^3v\frac{m}{2}v^2f\frac{\mathrm{d}\Psi}{\mathrm{d}t}\right\rangle, \tag{31}$$

$$Q_{\mathrm{pot}}=\left\langle\frac{1}{|\vec{\nabla}\Psi|}\int\mathrm{d}^3v\,q\phi f\frac{\mathrm{d}\Psi}{\mathrm{d}t}\right\rangle, \tag{32}$$

$$q_H=\left\langle\frac{1}{|\vec{\nabla}\Psi|}\int\mathrm{d}^3v\left[\frac{m}{2}(v^2-5v_{th}^2)+q\phi\right]f\frac{\mathrm{d}\Psi}{\mathrm{d}t}\right\rangle, \tag{33}$$

where $\mathrm{d}\Psi/\mathrm{d}t=\vec{\nabla}\Psi\cdot\mathrm{d}\vec{R}/\mathrm{d}t$ and $\langle\mathcal{A}\rangle=(1/S)\int_S\mathcal{A}\,\mathrm{d}\sigma$ is defined as the poloidal flux-surface-average of a quantity $\mathcal{A}$, S being the surface value. In practice, to ensure sufficient statistical accuracy from the PIC approach, surface averages are replaced by volume averages using the relation $\langle\mathcal{A}\rangle=\langle|\vec{\nabla}\Psi|\mathcal{A}\rangle_{\Delta V}/\langle|\vec{\nabla}\Psi|\rangle_{\Delta V}$, where $\langle\mathcal{A}\rangle_{\Delta V}=\int_{\Delta V}\mathcal{A}\mathrm{d}^3x/\Delta V$ stands for the volume average over the small volume ΔV enclosed between two neighboring magnetic surfaces Ψ and $\Psi+\Delta\Psi$. The heat flux q_H can be written as:

$$q_H=Q_{\mathrm{kin}}+Q_{\mathrm{pot}}-\frac{5}{2}T\Gamma. \tag{34}$$

Note that the presented simulations take into account the potential energy flux for a relevant computation of the effective heat diffusivity,[27] defined as $\chi_H=q_H/(n|\nabla T|)$. Diffusivities are usually normalized with respect to the Gyro-Bohm (GB) units: $\chi_{GB}=c_s\rho_s^2/a$, where $c_s=\sqrt{ZT_e/m_i}$ is the sound speed and the sound Larmor radius is defined as $\rho_s=c_s/\Omega_i$, with T_e taken at the reference radial position $r/a=0.5$ and the cyclotron frequency $\Omega_i=ZeB/m_i$ evaluated using the magnetic field on axis.

The so-called neoclassical fluxes are obtained from the contributions $\delta f_{CM}\cdot\mathrm{d}\Psi/\mathrm{d}t|_0$ and $f_{CM}\cdot\mathrm{d}\Psi/\mathrm{d}t|_{E\times B}$ in Eqs. (30)–(33), while the so-called turbulent fluxes, the usual fluxes computed in collisionless gyrokinetic codes, are provided by the contribution $\delta f_{CM}\cdot\mathrm{d}\Psi/\mathrm{d}t|_{E\times B}$ to $f\cdot\mathrm{d}\Psi/\mathrm{d}t$. Here, one has introduced the $\vec{E}\times\vec{B}$ drift contribution to the radial velocity $\mathrm{d}\Psi/\mathrm{d}t|_{E\times B}=\vec{\nabla}\Psi\cdot\vec{v}_{E\times B}$ and the magnetic drift contribution to the radial velocity $\mathrm{d}\Psi/\mathrm{d}t|_0=\vec{\nabla}\Psi\cdot(\vec{v}_{\nabla B}+\vec{v}_c)$. The particle and kinetic energy fluxes associated to $f_{CM}\cdot\mathrm{d}\Psi/\mathrm{d}t|_0$ do vanish as f_{CM} represents a stationary state of the unperturbed collisionless system.

E. Magnetic equilibrium

The considered *ad hoc* equilibrium[28] consists of toroidal, axisymmetric, nested magnetic surfaces with circular, concentric, and poloidal cross-sections. In this case, the axisymmetric magnetic field is given by $\vec{B}=\vec{\nabla}\Psi\times\vec{\nabla}\varphi+F(\Psi)\vec{\nabla}\varphi$, assuming $\Psi=\Psi(r)$ with $\mathrm{d}\Psi/\mathrm{d}r=rB_0/\bar{q}(r)$, as well as $F=RB_\varphi=R_0B_0$, so that:

$$\vec{B}=\frac{B_0R_0}{R}\left(\hat{e}_\varphi+\frac{r}{R_0\bar{q}(r)}\hat{e}_\theta\right), \tag{35}$$

where R is the major radius, r is the local minor radius, φ is the toroidal angle, θ is the poloidal angle, and $\hat{e}_\varphi,\hat{e}_\theta$ are the unit vectors in the toroidal and poloidal directions, respectively. The transformation between the toroidal variables

Downloaded 12 Apr 2012 to 128.178.234.18. Redistribution subject to AIP license or copyright; see http://pop.aip.org/about/rights_and_permissions

(r, φ, θ) and the cylindrical variables (R, φ, z) is provided by $R = R_0 + r\cos\theta$ and $z = r\sin\theta$. Furthermore, B_0 and R_0 stand for the magnetic field amplitude and major radius on the magnetic axis ($r = 0$). The $\bar{q}$ profile is chosen quadratic: $\bar{q}(r) = \bar{q}_0 + \bar{q}_1 r^2/a^2$, which is related to the safety factor profile $q_s(r)$ by the relation $\bar{q}(r) = \sqrt{1-\epsilon^2}q_s(r)$, where $\epsilon = r/R_0$ is the local inverse aspect ratio. The values $\bar{q}_0 = 0.854$ and $\bar{q}_1 = 2.184$ have been chosen such that $\bar{q}(r/a = 0.5) = 1.4$ and the magnetic shear $(r/\bar{q})\mathrm{d}\bar{q}/\mathrm{d}r|_{r=0.5a} = \hat{s}(r/a = 0.5) = 0.8$.

F. Physical parameters

For the simulation results presented in this paper, the physical parameters are inspired by the DIII-D shot underlying the CYCLONE test case[29] and similar to the parameters considered in Refs. 13 and 14. The considered aspect ratio is $a/R_0 = 0.36$, where a is the global minor radius. Choosing $T_e(r) = T_i(r)$ and Deuterium as the ion species, the size of the plasma is set at $a/\rho_s = 180$, where ρ_s is the sound Larmor radius defined in Sec. II D. Let $\mathcal{A}$ stand for either the temperature T or density n of a given species. Profiles are defined with respect to the coordinate r, with a flat logarithmic gradient:

$$\frac{\mathrm{d}\ln\mathcal{A}}{\mathrm{d}(r/a)} = -\frac{\kappa_\mathcal{A}}{2}\left[\tanh\left(\frac{r-(r_0-\Delta_\mathcal{A})}{\Delta_r}\right) - \tanh\left(\frac{r-(r_0+\Delta_\mathcal{A})}{\Delta_r}\right)\right], \tag{36}$$

where the values $r_0 = 0.5a$ for the center of the gradient profile and $\Delta_r = 0.04a$ for the width of the ramps have been chosen. Two actual gradient profile widths are considered: a narrow one with $\Delta_\mathcal{A} = 0.15a$ and a wide one with $\Delta_\mathcal{A} = 0.3a$. For the density profile $\kappa_n = 0.789$ such that $R_0/L_n = R_0\kappa_n/a = 2.2$ at $r = r_0$. Several temperature gradients ranging from $R_0/L_{T_0} = 4.5$ up to $R_0/L_{T_0} = 7.5$ are studied in the Secs. III–VI. The physical collisionality (see Eq. (23)) at $r = r_0$ for the CYCLONE case parameters is $\nu^*_{\mathrm{phys}} \simeq 0.045$. Collisionalities larger than the physical one, ranging from $2\nu^*_{\mathrm{phys}}$ up to $10\nu^*_{\mathrm{phys}}$, are studied in this paper, in order to emphasize the effects of collisions on the system.

G. Numerical parameters

The grid in configuration space chosen for solving the quasi-neutrality equation in this system is $N_r \times N_{\theta^*} \times N_\varphi = 128 \times 512 \times 256$, where N_r, N_{θ^*}, and N_φ are the number of grid points in the radial, poloidal, and toroidal direction, respectively. The size of the binning grid in (energy E, pitch angle ξ) velocity space for the coarse-graining procedure described in Sec. III is $n_E \times n_\xi = 40 \times 40$ in Sec. III and $n_E \times n_\xi = 64 \times 64$ in Secs. V and VI. For the turbulent simulations, only every second toroidal Fourier mode of the solution given by Eq. (27) is retained, namely $n = 0, 2, 4, \ldots, 56$, corresponding in real space to restricting the system to a toroidal wedge of half the full torus. A time step of $\Delta t = 0.22[a/c_s]$ is chosen. For the CYCLONE case described above, the number of markers ranges typically from $\sim 100 \times 10^6$ for collisionless runs up to 500×10^6 for collisional runs.

III. CONTROLLING NUMERICAL SAMPLING NOISE IN COLLISIONAL SIMULATIONS

A. Fourier filtering and signal-to-noise ratio (SNR) estimate

Numerical sampling noise is diagnosed in ORB5 by examining the spatially averaged squared density fluctuation amplitude in non-resonant, high-$k_{||}$ turbulent modes, which are physically supposed to be strongly Landau damped. These latter modes are thus at the limit or even beyond the gyrokinetic ordering, and only arise due to sampling errors.[30] Here, $k_{||} \simeq (nq_s - m)/Rq_s$ is the component of the wave vector of a given poloidal-toroidal Fourier mode (m, n) parallel to the magnetic field. Let us point out that the Fourier modes are computed using a straight-field-line poloidal angle θ^*. Invoking the fact that microturbulence is essentially aligned along the magnetic field lines, the charge density is Fourier-filtered, i.e., the quasi-neutrality solver retains only the Fourier modes (m, n), which at a given radial position Ψ, are such that $|nq_s(\Psi) - m| \leq \Delta m$, where $\Delta m = 5$ is typically used. Due to the validity range of the long wavelength approximation, the upper boundary for the toroidal Fourier modes n is typically chosen such that $k_\theta\rho_{Li} \simeq nq_s(r_0)\rho_{Li}/r_0 \leq 0.8$. In order to define a signal-to-noise ratio, the following definitions are introduced: the signal is estimated by the energy in the modes inside a certain Fourier filter $\mathcal{F}$ (low-$k_{||}$ modes), while the noise is estimated by the modes outside the Fourier filter (high-$k_{||}$ modes):

$$\begin{aligned}\text{signal} &= \frac{1/a\int_0^a dr\sum_{(n,m)\in\mathcal{F}}|\delta n^{(n,m)}(r)|^2}{\sum_{(n,m)\in\mathcal{F}}},\\ \text{noise} &= \frac{1/a\int_0^a dr\sum_{(n,m)\notin\mathcal{F}}|\delta n^{(n,m)}(r)|^2}{\sum_{(n,m)\notin\mathcal{F}}},\end{aligned} \tag{37}$$

where the energy-like estimates are computed on the basis of the density fluctuations. The Fourier components outside the filter $\mathcal{F}$ are removed from the density fluctuations before computing the electrostatic field. This is the basic noise-control procedure. If the noise becomes large compared to the physical signal, the simulations become irrelevant and are not further carried out. The critical level of the SNR which is considered to provide relevant results was empirically found to be SNR $\simeq 10$. In this paper, we describe an additional noise-control procedure in ORB5 for collisional runs, the so-called coarse-graining method, first proposed in Ref. 9 and further simplified in Ref. 10.

B. Coarse-graining

The purpose of the coarse-graining is to reduce the numerical noise, by filtering the high-k modes both in configuration and velocity space in case of a collisionless run and/or by reducing the weight spreading in case of a collisional run.[9] The aim of this procedure is to enable to maintain the signal/noise ratio at a higher level than simulations without coarse-graining, while retaining the key physics from the simulation. At a given time step, the coarse-graining

Downloaded 12 Apr 2012 to 128.178.234.18. Redistribution subject to AIP license or copyright; see http://pop.aip.org/about/rights_and_permissions

procedure involves: (1) the binning of the markers in the whole gyrokinetic phase space, i.e., a 5D binning and (2) the smoothing of the marker weights within a same bin, consisting of assigning the marker weights to their average value.

1. Binning

Let us describe the critical choice of the bin sizes and number of marker particles. In every direction of phase space, coarse-graining in effect damps any fluctuation scale which is of the order or below the corresponding bin size. This damping, being unphysical, must therefore apply to scales which do not contribute significantly to turbulent transport. This constraint thus fixes an upper limit on the size of bins. A practical choice for an appropriate coordinate system and grid resolution for defining the bins is provided by the meshes used in Eulerian-based gyrokinetic codes.[31] However, for the coarse-graining to be effective, one must ensure that every marker meets sufficiently often at least one other marker in a same bin at the same time step. This constraint in turn sets a lower limit on the number of required markers for a given number of bins. One must emphasize, however, that coarse-graining need not apply to each marker at each time step. Such a constraint would naturally compromise any advantage of a PIC method versus an Eulerian approach. Practice has shown that, on average, markers need only to undergo an effective coarse-graining procedure (i.e., meet at least one other marker in the same bin) every n-th time step for this noise control method to be efficient, where typically $n \sim 10$. As a result, the required ratio of marker number to bin number must be (at least) of order $1/n \sim 1/10$.

Let us define the normalized kinetic energy $E = v^2/2T(r)$ and the pitch angle $\xi = v_{||}/v$. Note that the energy dimension depends on the radial coordinate through the temperature profile $T(r)$. A uniform grid in θ^* is first built, leading to N_{θ^*} bins. Let us write $\theta_0^*(\theta^*)$ the function giving the position of the bin center θ_0^* corresponding to θ^*:

$$\theta_0^*(\theta^*) = \left[\mathrm{FLOOR}\left(\frac{\theta^* + \pi}{\Delta\theta^*}\right) + \frac{1}{2}\right]\Delta\theta^* - \pi, \qquad (38)$$

where $\theta^* \in [-\pi; \pi]$ and $\Delta\theta^* = 2\pi/N_{\theta^*}$ is the width of the bins along θ^*. FLOOR(x) stands for the largest integer which is smaller or equal to x. We define a new field-aligned coordinate z:

$$z = \varphi - q_s(s)[\theta^* - \theta_0^*(\theta^*)], \qquad (39)$$

where q_s is the safety factor and $s = \sqrt{\Psi/\Psi_{\mathrm{edge}}}$ is a normalized radial coordinate. Note that this field-aligned coordinate enables to use the largest possible bins in the θ^* direction, which now parametrizes the position along the field line. Indeed in the coordinates (s, θ^*, z), the dependence with respect to θ^* of a field-aligned fluctuation quantity represents the slowly varying envelope along the magnetic line. The fast phase variation transverse to the magnetic field is represented by both s and z. The binning is then defined as a block-structured Cartesian grid in the new set of variables (s, θ^*, z, E, ξ). The number of bins in the θ^* direction is proportional to the radial coordinate s ($s\Delta\theta^* \sim$ const.) in order to have bins of approximately the same volume, including near the magnetic axis, which is the center of the polar-like coordinates (s, θ^*). Figure 1 shows how the binning follows the field lines in the (θ^*, φ) plane, as well as the bin structure in the (θ^*, z) plane and in the (θ^*, s) plane.

2. Smoothing

Let us write α the general index identifying a 5D bin. Considering the bin α, we define the averaged w-weight and p-weight for the markers with index r present in the bin α at a given time:

$$\bar{w}_\alpha(t) = \frac{1}{N_\alpha}\sum_{r\in\alpha} w_r(t), \qquad (40)$$

$$\bar{p}_\alpha(t) = \frac{1}{N_\alpha}\sum_{r\in\alpha} p_r(t), \qquad (41)$$

where N_a is the number of markers in the bin α. Let us consider a marker r in a bin α. Introducing the relaxation rates γ_w and γ_p, the modification brought to both weights of the marker r after a coarse-graining procedure is:

$$\Delta w_r = \mathcal{N}\Delta t \cdot \gamma_w \cdot (\bar{w}_\alpha - w_r), \qquad (42)$$

$$\Delta p_r = \mathcal{N}\Delta t \cdot \gamma_p \cdot (\bar{p}_\alpha - p_r), \qquad (43)$$

where $\mathcal{N}$ is the number of time steps of length Δt between which coarse-graining is performed. The typical parameters for the simulations presented in this paper are $\mathcal{N} = 10$, $\gamma_w = 0.45[c_s/a]$ and $\gamma_p = 0.045[c_s/a]$. The chosen values are specific to given physical quantities, like the growth rate of the instability or the collisionality, and are not universal. The only mandatory requirement is $\mathcal{N}\Delta t \cdot \gamma \leqslant 1$. A full relaxation of all weights in a bin to the averaged weight value corresponds to $\mathcal{N}\Delta t \cdot \gamma_w = \mathcal{N}\Delta t \cdot \gamma_p = 1$.

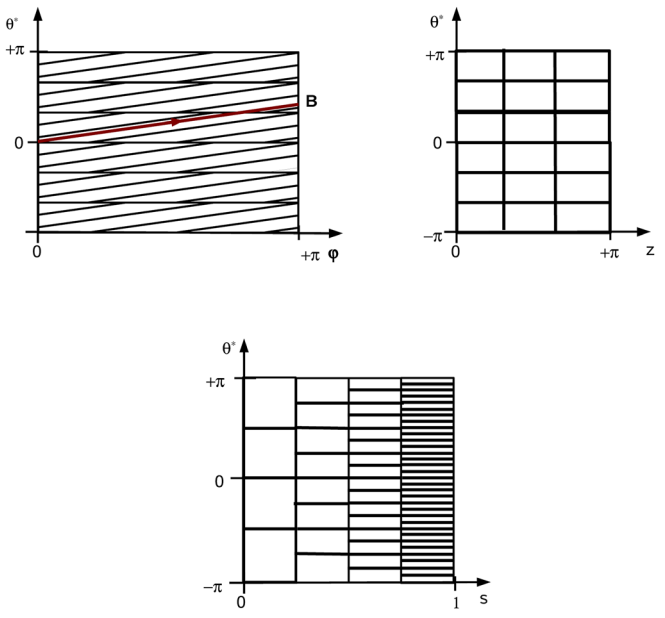

FIG. 1. Field-aligned binning in configuration space represented, respectively, in the (θ^*, φ) plane, the (θ^*, z) plane, and the (θ^*, s) plane.

Downloaded 12 Apr 2012 to 128.178.234.18. Redistribution subject to AIP license or copyright; see http://pop.aip.org/about/rights_and_permissions

C. Effects on turbulence

As already mentioned, the size of the bins needs to be chosen so as to be smaller than any scale length relevant to a correct estimation of the turbulent transport levels. Considering the CYCLONE base case described in Sec. II F with $R_0/L_{T_0} = 6.9$ and taking $n_s \times n_{\theta^*} \times n_z \times n_E \times n_\xi = 128 \times 32 \times 128 \times 40 \times 40$ as the binning grid for half of the torus (corresponding to a total of $\sim 840 \times 10^6$ bins), we first consider a non-heated plasma discretized with 100×10^6 markers. On average, each marker is thus expected to undergo an effective coarse-graining procedure every 10 time steps, 10 corresponding roughly to the ratio between the here considered number of bins and number of markers. Figure 2 shows that the coarse-graining procedure has no significant effect on the growth and non-linear saturation of different ITG modes, $n = 10$ and $n = 44$ corresponding, respectively, to $k_\theta \rho_{Li} \simeq 0.15$ and $k_\theta \rho_{Li} \simeq 0.68$. The latest result is in accordance with the purpose of the coarse-graining procedure, which is to reduce the numerical noise while not affecting scales relevant to turbulent transport. The size of the binning is, as expected, very important: if the bins are too large, significant scales of the turbulence are affected through the numerical damping of corresponding modes, as illustrated in Figure 2 for a number of bins reduced by a factor two in each direction. Let us emphasize again that this noise control method is fully compatible with the physics of collisions.[11] The self-induced zonal flows playing an essential role in the saturation of ITG turbulence, it is thus important to verify that their dynamics remain unaffected by the coarse-graining procedure as well. As these flows involve large scales, they are not expected to be directly affected by the potential damping of the binning process. They may, however, be indirectly affected by the flow drive, coming from the shorter scale fluctuation modes. This point is addressed in Figure 3 for the same conditions as in Figure 2, showing how the radially averaged $\vec{E} \times \vec{B}$ shearing rate $\langle |\omega_{E\times B}| \rangle_r$, defined by Eq. (45), is clearly unaffected in a time-average sense by the coarse-graining procedure.

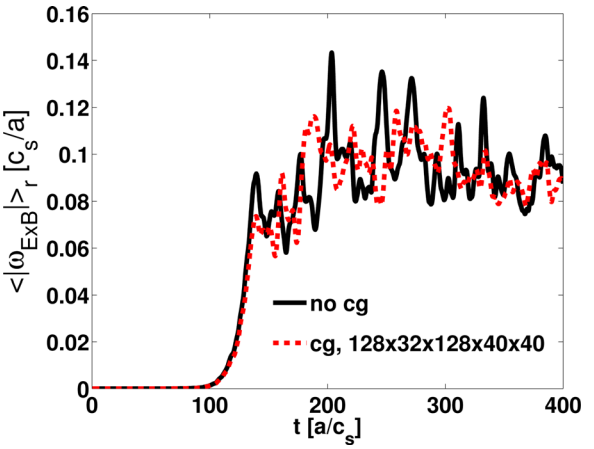

FIG. 3. Time evolution of the radially averaged $\vec{E} \times \vec{B}$ shearing rate $\langle |\omega_{E\times B}| \rangle_r$ without (plain line) and with (dashed line) coarse-graining: the coarse-graining procedure does not affect the time-average $\vec{E} \times \vec{B}$ flow shearing rate, as desired.

Considering the appropriate binning mentioned above, the positive effect of the coarse-graining is clearly illustrated in Figure 4, showing the signal/noise ratio for runs with either 90×10^6 or 180×10^6 markers, the heating operator being switched on. It has to be noticed from Figure 4 that the coarse-graining procedure is able to stabilize the signal/noise ratio. The simulations for which the noise is not controlled by the coarse-graining method indeed present a decaying signal/noise ratio in the time evolution, finally reaching a level below the threshold of simulation relevance (~ 10). The described coarse-graining procedure allows to carry out relevant, i.e., long enough studies of turbulence in the frame of the δf PIC method.

Note that the field-aligned coordinates are compatible with the gyrokinetic ordering (small $k_{||}\rho_{Li}$) and are thus the natural choice for representing micro-turbulence. Considering bins aligned along these coordinates enables to take the largest possible bins, essential for ensuring that every marker meets sufficiently often ($\sim$every 10 time steps) at least one

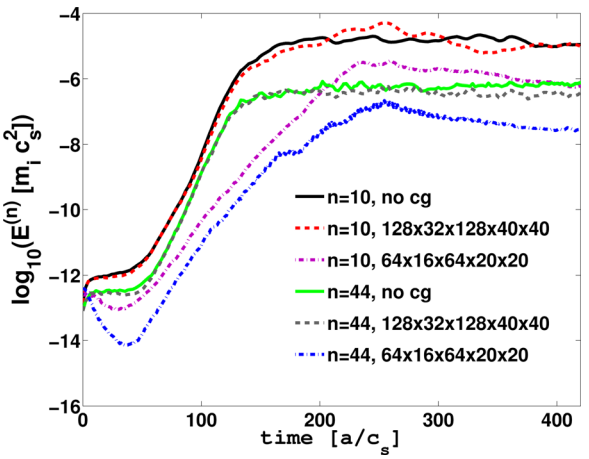

FIG. 2. Evolution in time of the energy $E^{(n)}$ of two toroidal Fourier modes ($n = 10$ and $n = 44$), for different coarse-graining parameters, in the linear phase and the early non-linear phase of the simulation. An appropriate choice of the coarse-graining binning parameters allows to preserve the linear growth rate of the modes, while too large bins lead to an important non-physical energy dissipation.

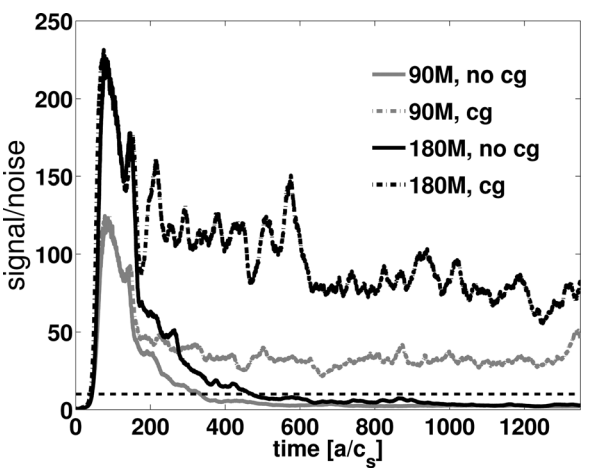

FIG. 4. Time evolution of the signal-to-noise ratio considering the coarse-graining procedure switched off (plain lines) and on (dash-dotted lines), respectively, both for 90×10^6 (grey lines) and 180×10^6 (black lines) markers. The coarse-graining method is crucial in order to carry out simulations above the SNR threshold of relevance ($\sim$ 10, dashed line).

Downloaded 12 Apr 2012 to 128.178.234.18. Redistribution subject to AIP license or copyright; see http://pop.aip.org/about/rights_and_permissions

other marker in a same bin at the same time step, while avoiding the coarse-graining procedure to smooth out essential physical scale lengths. This is illustrated by the number of bins considered in configuration space ($128 \times 32 \times 128$ for half of the torus) versus the number of grid points considered in straight-field-line coordinates for the field solver ($128 \times 512 \times 128$ for half of the torus).

IV. COLLISIONAL ROSENBLUTH-HINTON TESTS

This section points out essential differences between collisionless and collisional behaviour of the zonal flows by showing some results related to the so-called RH test.[5,32] The standard parameters given in Sec. II F are considered, except that temperature and density profiles with a peaked shape, as described by Eq. (43) of Ref. 11, are used in this section. In order to carry out RH tests, a local Maxwellian background $f_0 = f_{LM}$ is chosen for both the collisionless and collisional dynamics, and an initial distribution perturbation $\delta f_{LM} = (\delta n/n_0)\cos(\pi r/a) f_{LM}$ is loaded. The system is then linearly evolved by retaining only the axisymmetric component ($n = 0$ modes) of the electrostatic potential. In collisionless simulations, after relaxation of geodesic acoustic modes (GAMs) oscillations, the residual value of the radial electric field is proportional to the initial amplitude of the perturbation,[32] in both cases where profile gradients are or are not considered. In collisional simulations, the situation is fundamentally different: the zonal flows are damped as a result of collisions between passing and trapped ions[5] and the radial electric field always relaxes towards the neoclassical equilibrium value, which is non-zero for finite background profile gradients, regardless of the initial electric field amplitude. As expected, the neoclassical equilibrium field does vanish if no gradients are considered. Figures 5 and 6 illustrate these different scenarios by presenting the time evolution of the radial electric field $E_r(t)$ at $r/a = 0.5$, for both zero and non-zero CYCLONE case density and temperature gradients.

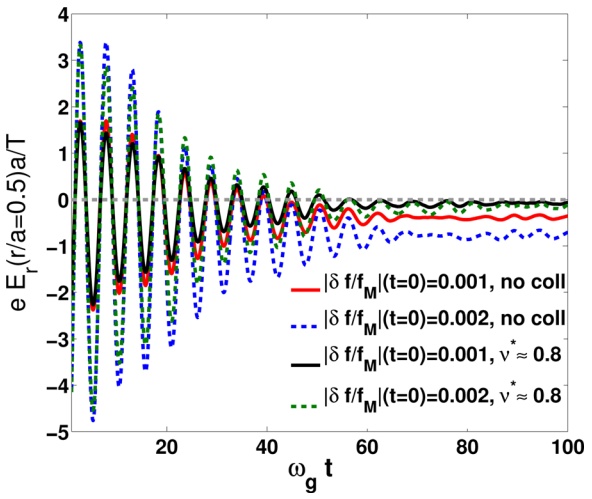

FIG. 5. Rosenbluth-Hinton test where no gradients are considered: time evolution of the radial electric field E_r at mid-radius for both collisionless and collisional simulations. The collisionless residual depends on the initial amplitude of the perturbation $|\delta f/f_{LM}|$, while the collisional residual does always vanish. Time is normalized by the GAM frequency ω_g.

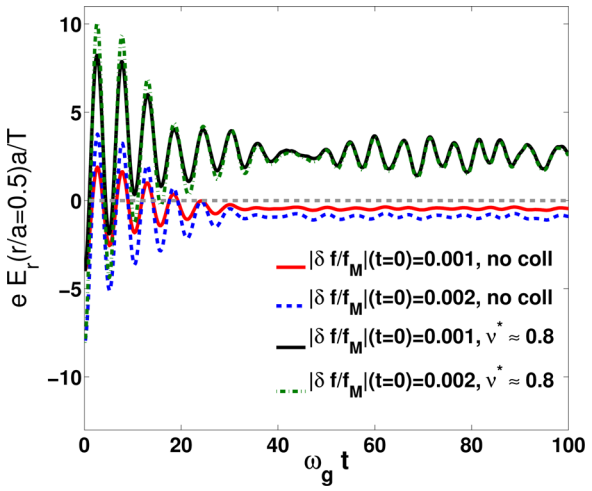

FIG. 6. Rosenbluth-Hinton test where the CYCLONE case gradients ($R_0/L_{n_0} = 2.2$, $R_0/L_{T_0} = 6.9$) are considered: time evolution of the radial electric field E_r at mid-radius for both collisionless and collisional simulations. The collisionless residual depends on the initial amplitude of the perturbation $|\delta f/f_{LM}|$, while the collisional residual converges towards the neoclassical equilibrium value, regardless of the initial perturbation. Time is normalized by the GAM frequency ω_g.

V. COLLISIONAL TURBULENT SIMULATIONS STARTED FROM A NEOCLASSICAL EQUILIBRIUM

Simulations have been carried out for collisionalities in the range $\nu_0^* = 0.09 - 0.45$, i.e., 2 to 10 times higher than the physical one $\nu_{\text{phys}}^* = 0.045$. Note that for studying collisional effects, simulations must be carried out over multiple collision times while resolving the shorter time scale of the turbulent fluctuations. Low collisionality is thus numerically challenging due to the large number of time steps required in order to reach a sufficient simulation time, while high collisionality is challenging as well due to the large number of markers required for ensuring a sufficient signal/noise ratio. Collisional simulations are performed with 500×10^6 markers representing the ions and started from a canonical Maxwellian as the total initial distribution: $f(t=0) = f_{CM}(\hat{\Psi})$. For collisional simulations, a first run with only axisymmetric modes ($n = 0$) is carried out over approximately two collision times τ_{ii}, in order to establish a neoclassical equilibrium with associated electric field and toroidal rotation profile. Note that the toroidal rotation profile of the neoclassical equilibrium is determined by the initial ion distribution function and may in principle affect, through its shearing, the development of turbulence in the subsequent simulation. As mentioned in Sec. II B 1, the choice of the background $f_{CM}(\hat{\Psi})$ has the purpose to provide neoclassical equilibria with essentially zero toroidal rotation. For the typical collisional CYCLONE cases considered here, the maximum toroidal velocity is $v_{\text{toro}} \sim 0.02 - 0.03 v_{thi}$ and the associated toroidal shearing rate is much smaller than the $\vec{E} \times \vec{B}$ shearing rate: $\omega_{\text{toro}} \sim 0.1 \omega_{E\times B}$.

In a second phase, the simulation is resumed taking into account both the axisymmetric and the non-axisymmetric modes ($n = 0$ and $n \neq 0$), thus allowing turbulence to develop and enabling to study the resulting anomalous transport and in particular the interaction between turbulence, neoclassical background flows, and turbulence-induced zonal flows. The

Downloaded 12 Apr 2012 to 128.178.234.18. Redistribution subject to AIP license or copyright; see http://pop.aip.org/about/rights_and_permissions

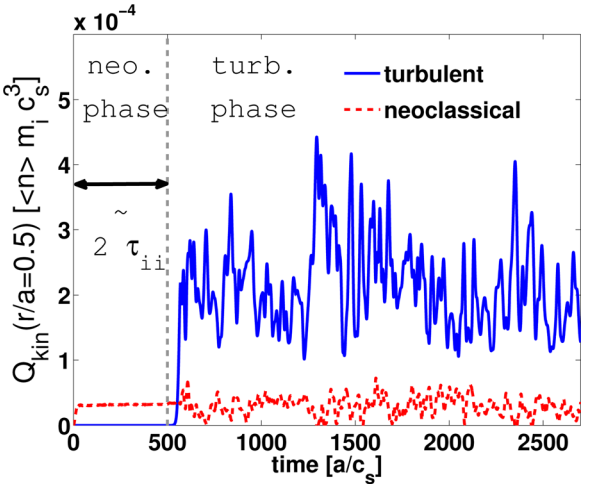

FIG. 7. Time evolution of the neoclassical (red dashed line) and turbulent (blue plain line) contributions to the kinetic energy flux Q_{kin} at mid-radius, in the neoclassical phase ($t < 500[a/c_s] \sim 2\tau_{ii}$) and the turbulent phase ($t > 500[a/c_s]$) of the simulation, for $\nu_0^* = 0.18$. Once a neoclassical equilibrium is established, turbulence is switched on and turbulent transport becomes dominant compared to neoclassical transport, for the here considered CYCLONE case gradients ($R_0/L_{n_0} = 2.2$, $R_0/L_{T_0} = 6.9$). The neoclassical flux is perturbed by turbulence but remains constant in a time-average sense.

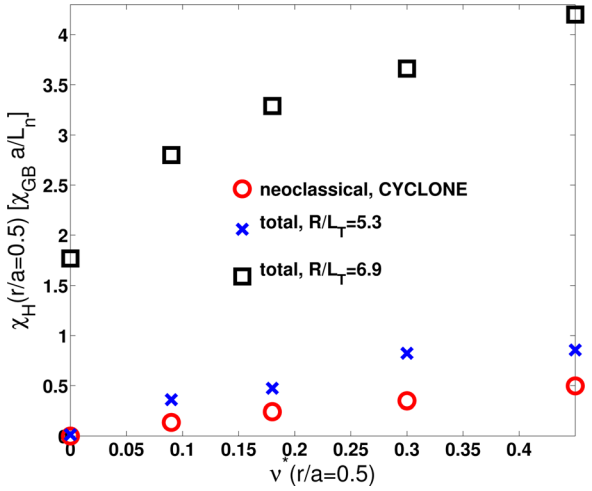

FIG. 8. Heat diffusivity χ_H at mid-radius versus the collisionality parameter ν^*, for both temperature gradients $R_0/L_{T_0} = 5.3$ (blue crosses) and $R_0/L_{T_0} = 6.9$ (black squares). The contribution of the neoclassical diffusivity (red circles) to the total diffusivity is important for the weaker gradient $R_0/L_{T_0} = 5.3$, while it becomes marginal for the larger gradient $R_0/L_{T_0} = 6.9$. The total diffusivity, increasing with collisions, is in all cases larger than the neoclassical diffusivity added to the collisionless turbulent diffusivity.

typical time evolution of the neoclassical and turbulent contributions to the kinetic energy flux Q_{kin} (as defined in Sec. II D), both in the neoclassical and turbulent phases of the simulation, is shown in Figure 7 for the temperature gradient $R_0/L_{T_0} = 6.9$ and collisionality $\nu_0^* = 4\nu_{\text{phys}}^* = 0.18$. The use of the heat source described by Eq. (25) enables to reach a quasi-stationary level of transport by maintaining a constant temperature gradient, in a time-average sense.

A. Heat diffusivity: Temperature gradient and collisionality effects

In this section, two temperature gradients are first considered, along with wide non-zero gradient profiles ($\Delta_{\mathcal{A}} = 0.3a$) for carrying out a collisionality scan. The first one, $R_0/L_{T_0} = 5.3$, is above the linear stability threshold $R_0/L_{T_0} \simeq 4.5$, but below the collisionless non-linear stability threshold $R_0/L_{T_0} \simeq 6.0$ of ITG turbulence in the considered physical system, i.e., in the so-called Dimits shift region.[29] The second one, $R_0/L_{T_0} = 6.9$, is above the non-linear stability threshold and thus ensures a stronger drive for the turbulence.

Figure 8 shows the neoclassical heat diffusivity χ_H^{neo} and the quasi-stationary total (neoclassical + turbulent) heat diffusivity $\chi_H^{\text{tot}} = \chi_H^{\text{neo}} + \chi_H^{\text{turb}}$ at mid-radius with respect to the collisionality. For the gradient below the non-linear stability threshold, $R_0/L_{T_0} = 5.3$, a non-vanishing turbulent transport illustrating a softening of the Dimits shift region is established through collisions. The turbulent diffusivity is relatively small in this latter case, i.e., of the order of the neoclassical diffusivity at each collisionality ($\chi_H^{\text{turb}} \sim \chi_H^{\text{neo}}$ such that $\chi_H^{\text{tot}} \sim 2\chi_H^{\text{neo}}$). Note that, as expected, there is zero transport at $R_0/L_{T_0} = 5.3$ if the collisions are switched off $[\chi_H(\nu^* = 0, R_0/L_{T_0} = 5.3) = 0]$. For the higher temperature gradient $R_0/L_{T_0} = 6.9$, the increase of the total diffusivity due to collisions is significantly larger than for $R_0/L_{T_0} = 5.3$ $[\chi_H^{\text{turb}}(\nu^*) - \chi_H^{\text{turb}}(\nu^* = 0) > \chi_H^{\text{neo}}(\nu^*)]$. For all gradients above the linear stability threshold, one thus observes:

$$\chi_H^{\text{tot}}(\nu^*) > \chi_H^{\text{turb}}(\nu^* = 0) + \chi_H^{\text{neo}}(\nu^*). \tag{44}$$

In general, the heat transport in the presence of both turbulence and ion-ion collisions is thus larger than the sum of collisionless turbulent and neoclassical transport considered separately. This reflects the complex interplay between collisional effects, flows, and turbulence.

Figure 9 presents the radial profiles of the quasi-stationary diffusivity χ_H for the particular collisionality case

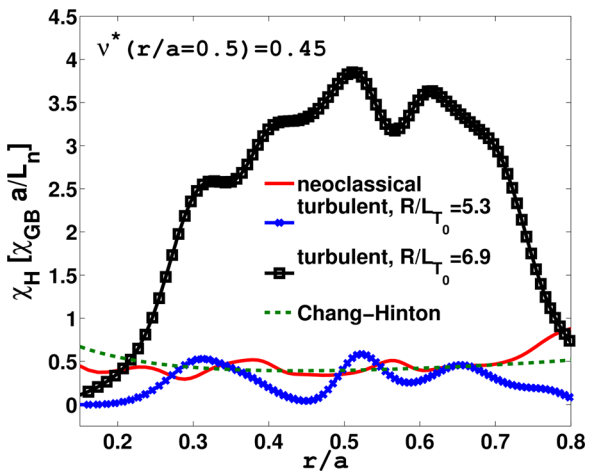

FIG. 9. Heat diffusivity profile $\chi_H(r)$ in the quasi-stationary state of the simulation, for a collisionality $\nu_0^* = 0.45$ and both temperature gradients $R_0/L_{T_0} = 5.3$ and $R_0/L_{T_0} = 6.9$. For the weaker gradient $R_0/L_{T_0} = 5.3$, the turbulent contribution profile (blue crosses) is similar to the neoclassical contribution profile (red plain line), while the turbulent contribution profile in the case of the larger gradient $R_0/L_{T_0} = 6.9$ (black squares) is clearly dominant. The neoclassical contribution is successfully benchmarked against the Chang-Hinton predictions (green dashed line).

Downloaded 12 Apr 2012 to 128.178.234.18. Redistribution subject to AIP license or copyright; see http://pop.aip.org/about/rights_and_permissions

$\nu_0^* = 10\nu_{phys}^* = 0.45$. The neoclassical contribution computed during the turbulent phase is compared to an analytical prediction derived by Chang and Hinton,[33] showing a good agreement. While the turbulent transport is of the order of the neoclassical transport in the case of the lower gradient $R_0/L_{T_0} = 5.3$, it becomes clearly dominant for $R_0/L_{T_0} = 6.9$.

The scan of considered temperature gradients is then extended at fixed collisionality, in order to sketch the dependence of the collisional heat diffusivity on the ion temperature gradient. Similar to studies already done for the CYCLONE parameters in the frame of collisionless simulations,[29] Figure 10 shows how the ion temperature gradient affects the ion heat diffusivity for ITG turbulence at mid-radius $r/a = 0.5$, for the chosen collisionality $\nu^* = 0.09 = 2\nu_{phys}^*$ as well as for the collisionless situation for reference. The blue plain line in Figure 10 is the fit to collisionless simulation results given in Ref. 29. While the Dimits shift softening is again clearly illustrated by the difference between neoclassical diffusivity and total collisional diffusivity in the collisionless Dimits shift region ($4.5 \leq R_0/L_{T_0} < 6.0$), the collisional increase of the transport level is also emphasized in the region above the non-linear stability threshold ($R_0/L_{T_0} \geq 6.0$).

B. Zonal flows in collisional ITG turbulence simulations

As the ion-ion collisions have a marginal influence on the growth rate of the ITG modes in the linear phase of the simulation (a slight increase of the linear growth rate if the parallel momentum is correctly conserved by collisions[34]), it is expected that the effect of collisions on the turbulent ITG transport happens mainly through their damping effect on the zonal flows. Just as for the collisionless case, the study of the zonal flows is thus essential in order to get insight into the collisional turbulent transport. The standard picture of the interaction between zonal flows and turbulence is the following:[1,3] above the linear ion temperature gradient threshold for the ITG instability, turbulence starts to develop and

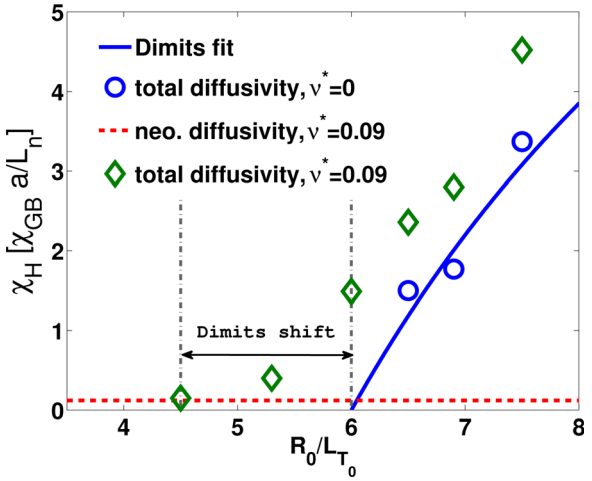

FIG. 10. Heat diffusivity χ_H at mid-radius versus the temperature gradient R_0/L_{T_0}. The blue plain line is the collisionless prediction resulting from an empirical fit on gyrokinetic simulation results. For $\nu_0^* = 0.09$, the red dashed line shows the neoclassical diffusivity level and the green diamonds represent the total diffusivity for different temperature gradients. Collisions clearly increase the heat diffusivity and soften the so-called Dimits shift region.

non-linearly drives zonal modes, which in turn tend to quench the turbulence due to the $\vec{E} \times \vec{B}$ shearing rate $\omega_{E\times B}$, given by the following approximate form:[35]

$$\omega_{E\times B} = \frac{r}{q_s B_0}\frac{\mathrm{d}}{\mathrm{d}r}\left(\frac{q_s E_r}{r}\right). \tag{45}$$

In order to deal with a global shearing rate, we define the radial average operator over the width $\Delta_{\mathcal{A}}$ of the gradient profiles:

$$\langle \ldots \rangle_r = \frac{1}{2\Delta_{\mathcal{A}}}\int_{r_0-\Delta_{\mathcal{A}}}^{r_0+\Delta_{\mathcal{A}}} \ldots \mathrm{d}r. \tag{46}$$

The maximum saturation level of zonal flows appears to be determined by a tertiary, Kelvin-Helmoltz (KH) type instability,[18] providing a mechanism for transferring energy back from zonal flows to turbulence. The KH saturation mechanism is illustrated in Figure 11(a), showing the time evolution of the radially averaged shearing rate $\langle|\omega_{E\times B}|\rangle_r$ for the CYCLONE base case with $R_0/L_{T_0} = 6.9$. In a first phase ($0 < tc_s/a < 130$), three collisionless simulations under the linear Rosenbluth-Hinton test conditions described in Sec. IV are performed, for different amplitudes of the initial perturbation: $|\delta f_{LM}/f_{LM}|(t=0) = 0.01, 0.05, 0.1$. The zonal flow residual and associated shearing rate amplitudes established after a time $t \simeq 130[a/c_s]$ are proportional to the initial amplitude of the perturbation, as expected and observed in Figure 11(a): $\langle|\omega_{E\times B}|\rangle_r = 0.04, 0.21, 0.42[c_s/a]$, respectively. In a second phase ($tc_s/a > 130$), the non-axisymmetric turbulent modes ($n \neq 0$) are enabled to evolve and interact with the axisymmetric zonal flows. The lowest initial amplitude case [$|\delta f_{LM}/f_{LM}|(t=0) = 0.01$] provides a residual zonal flow level clearly lower than the KH threshold level. Once the turbulence is switched on, it thus drives the zonal flows of the considered simulation to a higher level until the associated shearing rate reaches a saturation level of approximately $\langle|\omega_{E\times B}|\rangle_r \simeq 0.11[c_s/a]$, identified as the KH saturation level. For the higher amplitude cases [$|\delta f_{LM}/f_{LM}|(t=0) = 0.05, 0.1$], the shearing rate level of the residual zonal flow reached during the first phase of the simulation is clearly above the just mentioned KH saturation level. Once the non-axisymmetric modes ($n \neq 0$) are switched on, the axisymmetric modes transfer energy back to turbulence and the $\omega_{E\times B}$ shearing rate decays to the KH saturation level, $\langle|\omega_{E\times B}|\rangle_r \simeq 0.11[c_s/a]$, as observed in Figure 11(a). These results are clear proof of the tertiary instability threshold limiting the $\omega_{E\times B}$ shearing rate amplitude.

In order to fully isolate the KH instability mechanism limiting the shearing rate of the self-induced zonal flows, the previous runs are repeated with zero density and temperature gradients. In this case, the growth of $n \neq 0$ modes can thus only result from the decay of the zonal flows (ZF's) due to the tertiary instability, as the actual turbulent drive from the ITG instability has been removed. As shown in Figure 11(a), for the initial amplitude case $|\delta f_{LM}/f_{LM}|(t=0) = 0.05$, the shearing rate again decays once the $n \neq 0$ modes are turned on and the KH instability is enabled to evolve, from $\langle|\omega_{E\times B}|\rangle_r \simeq 0.21[c_s/a]$ at $t = 130[a/c_s]$ to $\langle|\omega_{E\times B}|\rangle_r \simeq 0.11[c_s/a]$, i.e.,

Downloaded 12 Apr 2012 to 128.178.234.18. Redistribution subject to AIP license or copyright; see http://pop.aip.org/about/rights_and_permissions

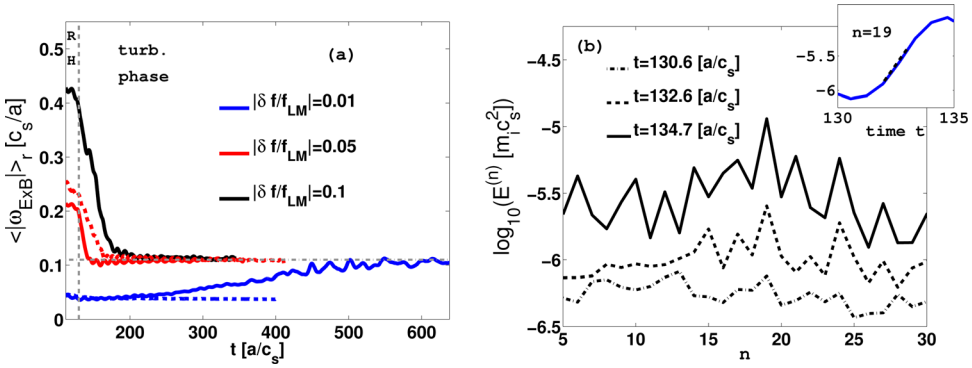

FIG. 11. Illustration of the KH saturation mechanism. (a) Time evolution of the radially averaged zonal flow shearing rate $\langle|\omega_{E\times B}|\rangle_r$ in non-linear collisionless simulations, following an initial linear $n=0$ phase (until $t \simeq 130[a/c_s]$) started at $t=0$ from $|\delta f/f_{LM}| = 0.01$, 0.05, and 0.1, respectively. With external turbulence drive from density and temperature gradients (plain lines), all three cases establish, in the long time scale, a similar level of zonal flow shearing rate. With no external turbulence drive (dashed lines), transfer of energy is only possible from zonal flows to turbulence. Note that the KH saturation level with or without external turbulence drive remains the same. (b) Growth of the $n \neq 0$ modes through zonal flow decay, for $|\delta f/f_{LM}|(t=0) = 0.1$ and no external turbulence drive. The most unstable mode is $n=19$ and its exponential growth phase is detailed in the inset.

to essentially the same KH threshold level observed in the presence of background gradients. For the initial amplitude case $|\delta f_{LM}/f_{LM}|(t=0) = 0.01$, the resulting shearing rate at $t = 130[a/c_s]$ again takes the value $\langle|\omega_{E\times B}|\rangle_r \simeq 0.04[c_s/a]$ as in the presence of gradients, i.e., lies below the KH threshold. As the turbulent drive of the zonal flows from the $n \neq 0$ modes is absent in this case, this shearing rate remains stationary as expected. The exponential growths of the $n \neq 0$ modes during the initial phase of the tertiary instability mechanism have been estimated. Modes in the range $n=17$–20 (corresponding to $k_\theta \rho_{Li} \simeq 0.26 - 0.31$) have been identified as the most unstable in this case. Evolution of the $n \neq 0$ modes during the KH instability is shown in Figure 11(b) for the initial amplitude case $|\delta f_{LM}/f_{LM}|(t=0) = 0.1$. A maximum growth rate $\gamma_{KH} = 0.55[c_s/a]$ for $n=19$ was measured for this latter case, while essentially half this growth rate is measured for $|\delta f_{LM}/f_{LM}|(t=0) = 0.05$, i.e., $\gamma_{KH} = 0.27[c_s/a]$ $(n=17)$, in very good agreement with theory[18] predicting that the KH growth rate is proportional to the amplitude of the zonal modes.

In a third phase, the simulation with gradients and the initial perturbation $|\delta f_{LM}/f_{LM}|(t=0) = 0.05$ is then resumed from $t \simeq 330[a/c_s]$, considering two different collisionalities $\nu_0^* = 0.09$ and $\nu_0^* = 0.45$ as presented in Figure 12. The average zonal flow level $\langle|\omega_{E\times B}|\rangle_r$ is as expected damped by collisions, but nevertheless maintained close to the collisionless value through additional drive from increased turbulence in collisional simulations, as presented in Sec. V A. Moreover, one observes that both collisionalities considered lead to approximately the same collisional level of the zonal flow shearing rate $\omega_{E\times B}$, reduced by $\sim 30\%$ compared to the collisionless value. In the first phase of the collisional simulation, the zonal flows are more strongly damped for the largest collisionality $\nu_0^* = 0.45$, but then increase in a second phase through additional turbulence kicks in order to reach roughly the same level as obtained with the moderate collisionality $\nu_0^* = 0.09$. As a consequence of the stronger turbulence drive, the radially averaged turbulent energy flux $\langle Q_{\text{turb}}\rangle_r$ for $\nu_0^* = 0.45$ is larger than for $\nu_0^* = 0.09$ $[\langle Q_{\text{turb}}\rangle_r(\nu_0^* = 0.45) / \langle Q_{\text{turb}}\rangle_r(\nu_0^* = 0.09) \simeq 1.8]$, in accordance with the collisional increase of the turbulent transport emphasized in Sec. V A.

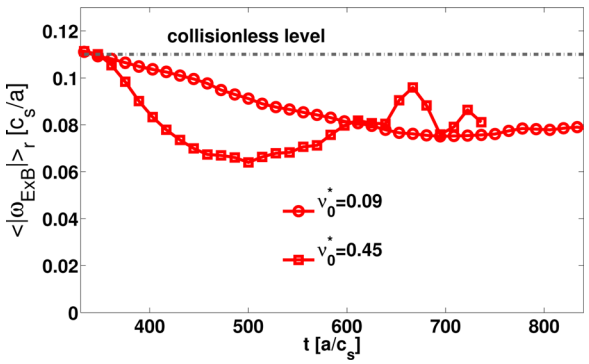

FIG. 12. Non-linear simulations resumed at $t \simeq 330[a/c_s]$ from the simulation in Fig. 11 started from $|\delta f/f_{LM}| = 0.05$, turning on finite collisionalities $\nu_0^* = 0.09$ (circles) and $\nu_0^* = 0.45$ (squares), respectively. A moderate reduction of the average zonal flow shear level $\langle|\omega_{E\times B}|\rangle_r$ by collisions is observed, roughly independent of the considered collisionality at sufficiently long time scales.

In absence of collisions, if the zonal shearing rate $\omega_{E\times B}$ is strong enough below or at its KH saturation level in order to quench the turbulence, as is the case for the temperature gradient $R_0/L_{T_0} = 5.3$, no turbulent transport occurs. On the contrary, if the drive is strong enough, as is the case for the temperature gradient $R_0/L_{T_0} = 6.9$, turbulence is not totally quenched by the saturated zonal flow shearing and some turbulent transport develops. The existence of a tertiary instability threshold setting a saturation level on the zonal flows thus explains the end of the Dimits shift region starting from $R_0/L_{T_0} \simeq 6.0$, where the turbulence drive becomes too large compared to the saturated zonal flow level and is thus able to produce finite anomalous transport. The latter mechanism is emphasized in Figure 13, which shows, respectively, $\langle|\omega_{E\times B}|\rangle_{r,t}$ and the maximum linear growth rate γ_{max} for different values of the temperature gradient R_0/L_{T_0}, considering the collisionless situation as well as the finite collisionality $\nu_0^* = 0.09$. Note that the considered collisionality has a negligible effect on $\gamma_{\max}$. The end of the Dimits shift region, at approximately $R_0/L_{T_0} \simeq 6.0$, is characterized by a maximum

Downloaded 12 Apr 2012 to 128.178.234.18. Redistribution subject to AIP license or copyright; see http://pop.aip.org/about/rights_and_permissions

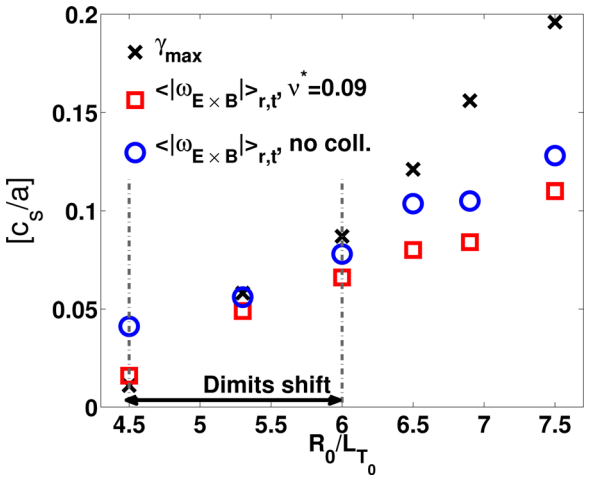

FIG. 13. Maximum linear growth rate γ_{max} (black crosses) and average shearing rate $\langle|\omega_{E\times B}|\rangle_{r,t}$, considering both the finite collisionality $\nu_0^* = 0.09$ (red squares) and a collisionless case (blue circles), for different temperature gradients R_0/L_{T_0}. Note that the average shearing rate is in general slightly reduced by collisions. Beyond the Dimits shift region, $\gamma_{max} > \langle|\omega_{E\times B}|\rangle_{r,t}$. The important difference between γ_{max} and $\langle|\omega_{E\times B}|\rangle_{r,t}$ at large temperature gradients is due to a tertiary instability mechanism.

linear growth rate γ_{max} which becomes larger than the average zonal flow shear level $\langle|\omega_{E\times B}|\rangle_{r,t}$. Note that the difference between $\gamma_{\max}$ and $\langle|\omega_{E\times B}|\rangle_{r,t}$ increases for temperature gradients $R_0/L_{T_0} > 6.0$, due to the mentioned tertiary instability mechanism, which limits $\langle|\omega_{E\times B}|\rangle_{r,t}$ and thus allows a stronger turbulence to develop at higher temperature gradients.

Consistently with Figure 12, the averaged shearing rate for basically all gradients is only slightly reduced by collisions (~20%), although, as predicted in Ref. 5 and as illustrated in Sec. IV, the zonal flows driven by turbulence are shown to be damped by ion-ion collisions. This effect is detailed in Tables I and II, for both temperature gradients $R_0/L_{T_0} = 5.3$ and $R_0/L_{T_0} = 6.9$, respectively, where the average shearing rate amplitudes $\langle|\omega_{E\times B}|\rangle_{r,t}$ are presented, including statistical error estimates given by the variance of means for 4 overlapping time windows of width $200[a/c_s]$ ($\sim 2\tau_{ii}$ for $\nu^* = 0.45$) in the quasi-stationary state of the simulation. These values are indeed only slightly reduced by finite collisionality over the whole considered range $\nu^* = 2 - 10\nu^*_{\text{phys}}$ and thus remain of the order of the collisionless level. The additional drive for zonal flows, coming from the increased turbulence observed in collisional simulations, thus appears to essentially compensate the damping by ion-ion collisions. For collisional runs in the Dimits shift region (including $R_0/L_{T_0} = 5.3$), the average shearing rates can only be maintained at approximately the collisionless levels thanks to a finite turbulence level, leading to finite transport and to the so-called Dimits shift softening. A tight equilibrium between zonal flow damping by collisions and zonal flow drive by additional turbulence is thus apparently established. In the absence of collisions, no such tight balance between damping and drive is imposed on the zonal flows, which are thus free to exceed the minimum required level for quenching turbulence in the Dimits shift region. This probably explains the larger difference between $\omega_{E\times B}$ for $\nu_0^* = 0$ and $\nu_0^* = 0.09$ at $R_0/L_{T_0} = 4.5$ than for other values of R_0/L_{T_0}.

TABLE I. Dependence on ν_0^* of average shearing rate $\langle|\omega_{E\times B}|\rangle_{r,t}$ for $R_0/L_{T_0} = 5.3$.

ν_0^*	0	0.09	0.18	0.3	0.45
$\langle\|\omega_{E\times B}\|\rangle_{r,t}[10^{-2}c_s/a]$	5.6 ± 0.09	4.9 ± 0.03	4.8 ± 0.03	5.2 ± 0.01	5.3 ± 0.03

TABLE II. Same as Table I but for $R_0/L_{T_0} = 6.9$.

ν_0^*	0	0.09	0.18	0.3	0.45
$\langle\|\omega_{E\times B}\|\rangle_{r,t}[10^{-2}c_s/a]$	10.5 ± 1.3	8.4 ± 0.4	9.5 ± 1.4	9.4 ± 0.5	9.5 ± 0.09

Figure 14 shows the profiles of the absolute $\vec{E}\times\vec{B}$ shearing rate values $|\omega_{E\times B}|(r)$, averaged over a time window of $200[a/c_s]$ in the quasi-stationary state of the turbulent simulation, for different collisionalities and for the temperature gradient $R_0/L_{T_0} = 5.3$. Considering this latter case in the Dimits shift region, the radially averaged shearing rate $\langle|\omega_{E\times B}|\rangle_r \simeq 5.2\times10^{-2}[c_s/a]$ (average over all ν^*) is close to the linear growth rate of the most unstable mode $\gamma_{max} \simeq 5.8\times10^{-2}[c_s/a]$, consistently with Figure 13. Furthermore, as mentioned above, the radially averaged shearing rate $\langle|\omega_{E\times B}|\rangle_r$ is only slightly affected by collisions. This is remarkable, given that the radial shearing rate profile $|\omega_{E\times B}|(r)$ is significantly modified when going from zero to finite collisionality. Note, however, the almost identical shape of $|\omega_{E\times B}|(r)$ for the two considered finite collisionalities $\nu_0^* = 0.09$ and $\nu_0^* = 0.18$.

Figure 15 is similar to Figure 14 but considers the higher temperature gradient $R_0/L_{T_0} = 6.9$. Considering this latter case above the Dimits shift region, $\gamma_{max} \simeq 15.6\times10^{-2}[c_s/a]$ is significantly larger than the shearing rate ($\langle|\omega_{E\times B}|\rangle_r \simeq 9.4\times10^{-2}[c_s/a]$, average over all ν^*), allowing the turbulence to survive and continuously drive anomalous transport, in accordance with Figures 10 and 13. As for $R_0/L_{T_0} = 5.3$,

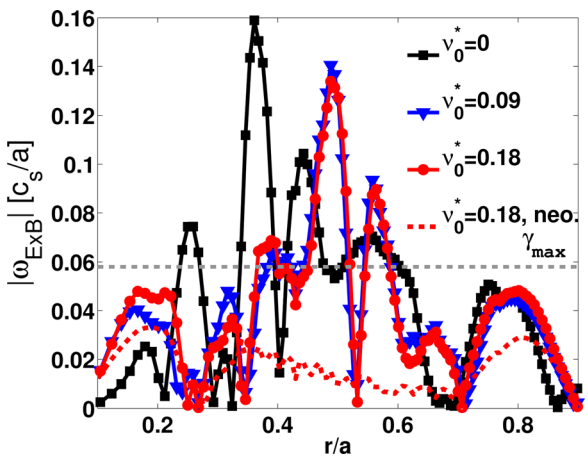

FIG. 14. Profiles of the $\vec{E}\times\vec{B}$ shearing rate absolute value $|\omega_{E\times B}|(r)$ for different collisionalities and a temperature gradient $R_0/L_{T_0} = 5.3$, the neoclassical contribution being emphasized. The average shearing rate level is of the order of the growth rate of the most unstable mode γ_{max} (grey dashed line). The zonal flow damping by collisions appears to be balanced by an additional turbulence drive. For the considered collisionalities, the turbulence-driven zonal flows are dominant compared to the neoclassical flows.

Downloaded 12 Apr 2012 to 128.178.234.18. Redistribution subject to AIP license or copyright; see http://pop.aip.org/about/rights_and_permissions

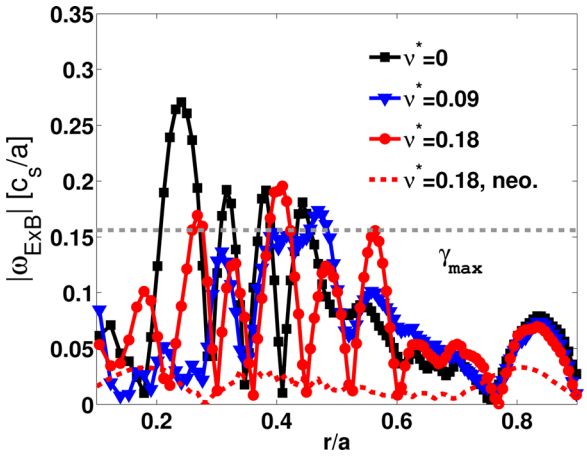

FIG. 15. Same representation as in Fig. 14, but considering a temperature gradient $R_0/L_{T_0} = 6.9$. The average shearing rate level is much smaller than the growth rate of the most unstable mode γ_{max} (grey dashed line). The collisional zonal flow amplitudes are only slightly reduced thanks to the additional turbulence drive. For the considered collisionalities, the turbulence-driven zonal flows are dominant compared to the neoclassical flows.

the amplitude of the collisional zonal flows appears to be only slightly reduced in the case $R_0/L_{T_0} = 6.9$ compared to the collisionless situation. The detailed shape of the profile $|\omega_{E\times B}|(r)$ is, however, affected by collisions and, unlike in the Dimits shift region, different collisionalities ($\nu_0^* = 0.09$ and $\nu_0^* = 0.18$) give different profiles $|\omega_{E\times B}|(r)$ for $R_0/L_{T_0} = 6.9$.

Note that ion-ion collisions generate neoclassical background flows through the neoclassical equilibrium electric field. For the collisionalities considered in this paper (up to $10 \times \nu^*_{\text{phys}}$), the turbulence-driven flows are dominant compared to the neoclassical background flows, as shown in Figures 14 and 15. At even larger collisionality, one may expect that the neoclassical shearing rate would become dominant, and thus that the turbulent transport would possibly be *reduced* due to collisions. However, such a high collisionality range would be very far from the typical low collisionality regimes of fusion-relevant tokamak plasmas.

C. Details of the Dimits shift softening mechanism

In Ref. 13, the zonal flow damping by collisions was first identified as the cause for the non-vanishing collisional turbulent transport for $R_0/L_{T_0} = 5.3$, although the temperature gradient is in the Dimits shift region. A locally bursting behaviour of turbulence, associated zonal flow amplitude, and turbulent transport was observed. The bursting behaviour results from the following mechanism: turbulence driven by the (weak) temperature gradients in the Dimits shift region initially develops and drives zonal flows to sufficiently high levels such that the associated shearing rate $\omega_{E\times B}$ is able to quench the turbulence, as in the collisionless case. As a result of collisional damping, zonal flow amplitudes and related shearing then, however, decrease, and turbulence is able to recover, thus completing a bursting cycle. The period of this bursting cycle therefore clearly scales with the collision time τ_{ii}. This result is confirmed by simulations performed with the collisional version of ORB5 based

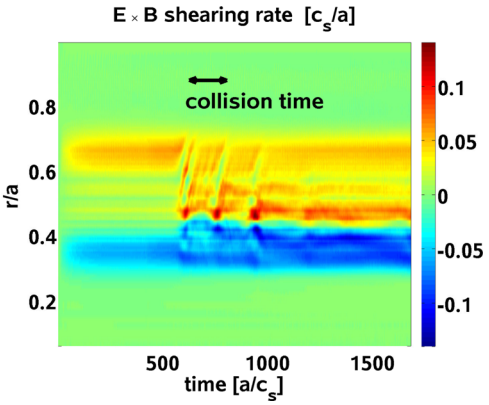

FIG. 16. Time evolution of the $\vec{E} \times \vec{B}$ shearing rate profile, considering a collisionality $\nu_0^* = 0.3$ and a temperature gradient $R_0/L_{T_0} = 5.3$. The temperature and density gradients are non-zero from $r/a = 0.35$ to $r/a = 0.65$ (narrow-shaped profiles, $\Delta_{\mathcal{A}} = 0.15a$). The bursting evolution of the zonal flows is visible.

on the parameters defined in Sec. II F for a *narrow* gradient profile, i.e., with $\Delta_{\mathcal{A}} = 0.15a$. Figure 16 shows the time evolution of the radial shearing rate profile $\omega_{E\times B}(r)$ for $\nu_0^* = 0.3$, considering a narrow gradient profile with $R_0/L_{T_0} = 5.3$. Note that the observation of a clear bursting behaviour, as in Figure 16, requires narrow gradients as those considered in this section. As an illustration, Figure 17 presents the time evolution of the radial shearing rate profile $\omega_{E\times B}(r)$ for $\nu_0^* = 0.3$ and considering a wide gradient profile, i.e., with $\Delta_{\mathcal{A}} = 0.3a$, and still with $R_0/L_{T_0} = 5.3$. In this latter case, discussed in Sec. V A, the bursting behaviour is much less obvious.

The bursting behaviour due to collisions for profile width $\Delta_{\mathcal{A}} = 0.15a$ and gradient $R_0/L_{T_0} = 5.3$ is clearly illustrated in Figures 18–20. As expected, transport is totally absent in a collisionless case, as shown in Figure 18 for $\nu^* = 0$, since the temperature gradient $R_0/L_{T_0} = 5.3$ is in the Dimits shift region, where the collisionless zonal flows are strong enough to quench the turbulence. Considering again $R_0/L_{T_0} = 5.3$ and two different collisionalities $\nu^* \simeq 0.18$ and $\nu^* \simeq 0.3$ at the radial position $r/a = 0.45$, Figures 19 and

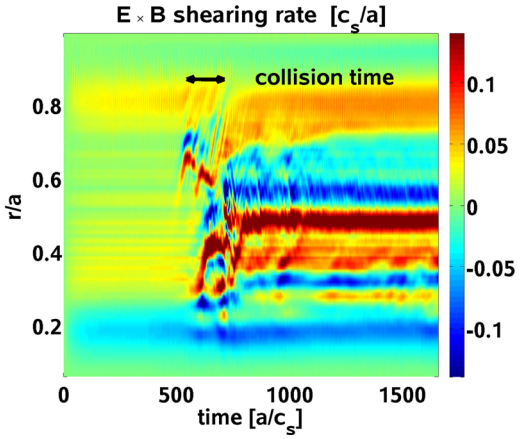

FIG. 17. Same representation as in Fig. 16, but considering temperature and density gradients which are non-zero from $r/a = 0.2$ to $r/a = 0.8$ (wide-shaped profiles, $\Delta_{\mathcal{A}} = 0.3a$). The bursting behaviour of the zonal flows is much less obvious than in Fig. 16.

Downloaded 12 Apr 2012 to 128.178.234.18. Redistribution subject to AIP license or copyright; see http://pop.aip.org/about/rights_and_permissions

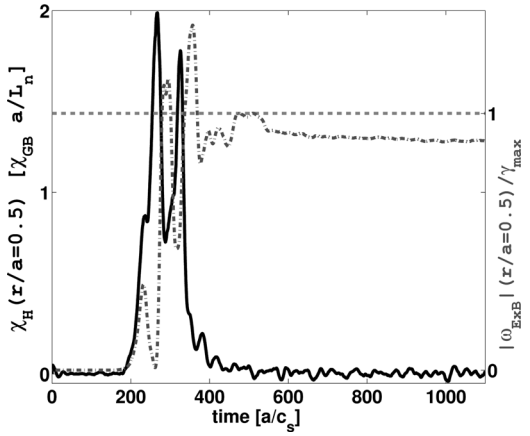

FIG. 18. For a collisionless simulation and a narrow temperature gradient with $R_0/L_{T_0} = 5.3$, time evolution of both the heat diffusivity χ_H (black plain line) and the $\vec{E} \times \vec{B}$ shearing rate $|\omega_{E\times B}|$ (grey dash-dotted line) at mid-radius. $|\omega_{E\times B}|$ reaches a quasi-stationary value comparable to the linear growth rate of the most unstable mode γ_{max} (grey dashed line), quenching totally the turbulence and leading to a vanishing heat transport.

20 show the time evolution of the turbulent ion energy flux Q_{turb}, normalized with respect to its corresponding neoclassical value Q_{neo}, as well as the time evolution of the $\vec{E} \times \vec{B}$ shearing rate $\omega_{E\times B}$, normalized with respect to the growth rate of the most unstable mode γ_{max} in the linear phase of the simulation. A non-vanishing turbulent transport is clearly established through collisions. The above mentioned bursting behaviour appears clearly in Figures 19 and 20: at an intermittent period which is proportional to the collision time τ_{ii} (indicated for reference in the figures), the $\vec{E} \times \vec{B}$ shearing rate is damped, which in turn leads to an increase of the turbulent ion energy flux. The observation of a non-vanishing turbulent transport implies that the Dimits shift region of ion temperature gradients is softened by collisions, as already discussed in Sec. V A for $\Delta_{\mathcal{A}} = 0.3a$ cases. As already mentioned, the observed bursting behaviour is, however, not as clearly identifiable if the gradient profiles are larger, maybe due to interaction of this bursting behaviour

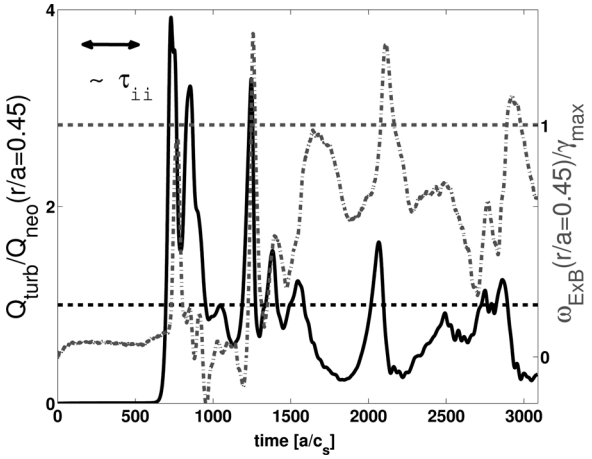

FIG. 19. For $\nu_0^* = 0.18$ and a narrow temperature gradient with $R_0/L_{T_0} = 5.3$, time evolution of both the kinetic energy flux driven by turbulence Q_{turb} (black plain line) and the $\vec{E} \times \vec{B}$ shearing rate $\omega_{E\times B}$ (grey dash-dotted line) at $r/a = 0.45$. The periodic damping of the zonal flows by collisions leads in turn to periodic bursts in the heat transport, at a rate proportional to the collision frequency.

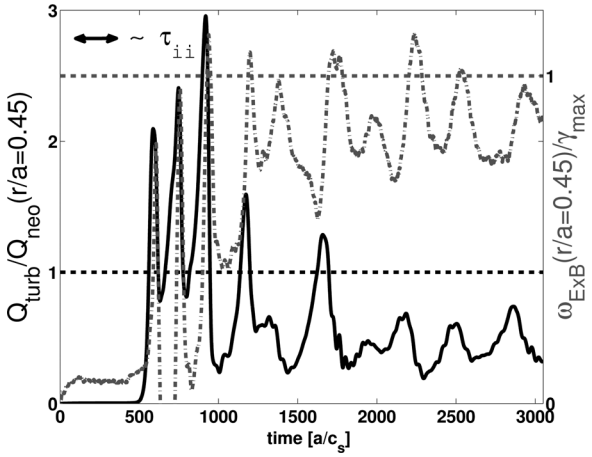

FIG. 20. Same representation as in Fig. 19 for $\nu_0^* = 0.3$, leading to the same conclusions. The periodicity of the observed bursting behaviour is again related to the collision frequency.

happening at different uncorrelated times at different radii, leading to a less coherent evolution of the overall system. The basic underlying mechanisms of turbulence-driven zonal flow damping are, however, probably essentially the same, leading to an increase of the diffusivity with collisions for all gradient widths.

VI. RELEVANCE OF THE PITCH ANGLE SCATTERING APPROXIMATION

Historically, collision operators have been implemented in gyrokinetic codes by making use of several approximations. Certain gyrokinetic codes for instance only consider a pitch angle scattering operator for turbulence studies.[12] The linearized Landau operator implemented in ORB5 for self-collisions, described in detail in Ref. 11, accounts for pitch angle and energy diffusion, and thanks to its approximated background reaction term ensures all the essential conservation and symmetry properties. In this respect, it is clearly more realistic than the simpler pitch angle scattering operator (Lorentz approximation). A pitch angle scattering operator for electron-ion collisions, acting only through random kicks for markers in the pitch angle variable, is also implemented in ORB5 and described in full detail in Ref. 11. Such an operator is clearly relevant for simulating the collisions of electrons on ions, due to the large mass ratio m_i/m_e between the two species. Such a mass ratio argument clearly does not apply for ion-ion collisions, which are thus different from electron-ion collisions, and the use of a pitch angle scattering operator for ion-ion collisions may be questioned. Using a Lorentz operator in order to account for self-collisions is equivalent to considering the linearized Landau self-collision operator without the background reaction term $C[\delta f_{LM}, f_{LM}]$ and without the energy diffusion term, such that the simplified self-collision operator reads (see Eq. (31) in Ref. 11):

$$\hat{C}(\delta f_{LM}) = \frac{\nu_D(v)}{2}\hat{L}^2\delta f_{LM} = \frac{\nu_{ii}K(\mathsf{v})}{4\mathsf{v}^2}\hat{L}^2\delta f_{LM}, \qquad (47)$$

where $\mathsf{v} = v/v_{th}, \hat{L}^2 = \partial/\partial\xi(1-\xi^2)\partial/\partial\xi$ and

Downloaded 12 Apr 2012 to 128.178.234.18. Redistribution subject to AIP license or copyright; see http://pop.aip.org/about/rights_and_permissions

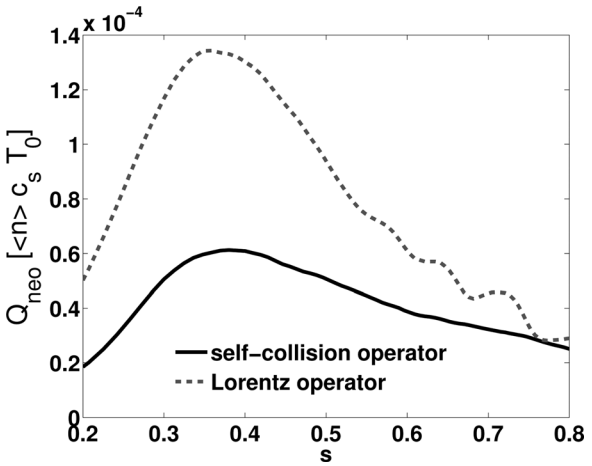

FIG. 21. For $\nu_0^* \simeq 0.71$ and $R_0/L_{T_0} = 5.3$, neoclassical kinetic energy flux profile due to ion-ion collisions $Q_{\text{neo}}(s)$ predicted by both the Lorentz operator (grey dashed line) and the Landau self-collision operator (black plain line). The Lorentz approximation is not accurate enough in order to describe correctly the neoclassical transport due to self-collisions.

$$K(\mathrm{v}) = \frac{1}{\mathrm{v}^3}\left[(\mathrm{v}^2-1)\mathrm{erf}(\mathrm{v}/\sqrt{2}) + \sqrt{2/\pi}\mathrm{v}e^{-\mathrm{v}^2/2}\right] \qquad (48)$$

is a Rosenbluth potential related function.

Considering the standard CYCLONE case with $R_0/L_{T_0} = 5.3$, a turbulent run started from a neoclassical equilibrium at very high collisionality $\nu_0^* \simeq 0.71$ is first studied. As expected, the neoclassical equilibrium to which the system settles with the Lorentz operator (47) is different from the equilibrium with the full self-collision operator (1). The neoclassical kinetic energy flux Q_{neo} predicted by the Lorentz operator is for instance larger than the neoclassical kinetic energy flux predicted by the Landau self-collision operator, as shown in Figure 21. Note that the neoclassical electric field is in some sense inconsistent in the case of the Lorentz operator, since the Lorentz operator does not conserve parallel momentum and thus leads to a neoclassical ion particle flux which is unphysical for self-collisions.[36] The neoclassical electric field, settled for ensuring a vanishing ion particle flux in order to satisfy the quasi-neutrality equation with adiabatic electrons, is thus distorted by the unphysical particle flux driven by the Lorentz operator. However, the use of the Lorentz operator in the frame of turbulence studies seems to be roughly justified. Despite evident neoclassical discrepancies, the time-averaged turbulent kinetic energy flux at mid-radius $r/a = 0.5$ remains comparable between the operators, $\langle Q_{\text{turb,Lorentz}}\rangle_{\text{time}}/\langle Q_{\text{turb,self-coll}}\rangle_{\text{time}} = 1.14$. Considering the statistical uncertainty of 15%,[8] this deviation is probably not significant. Figure 22 shows the evolution in time of the turbulent kinetic energy flux at mid-radius $r/a = 0.5$ for both operators.

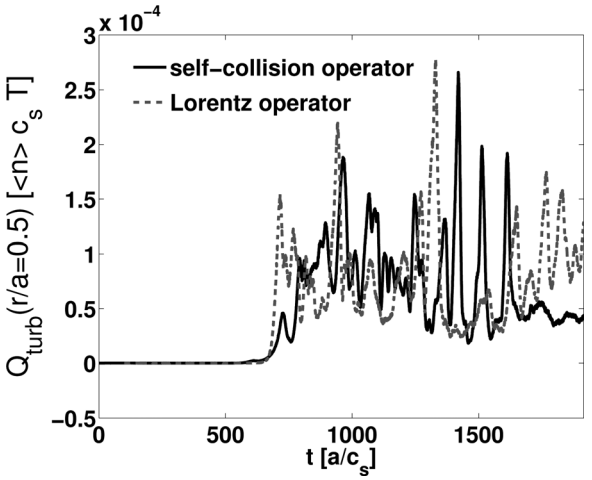

FIG. 22. For $\nu_0^* \simeq 0.71$ and $R_0/L_{T_0} = 5.3$, time evolution of the turbulent kinetic energy flux Q_{turb} at mid-radius predicted by both the Lorentz operator (grey dashed line) and the Landau self-collision operator (black plain line). Despite visible discrepancies, the level of turbulent transport is approximately described by the Lorentz operator in a time-average sense.

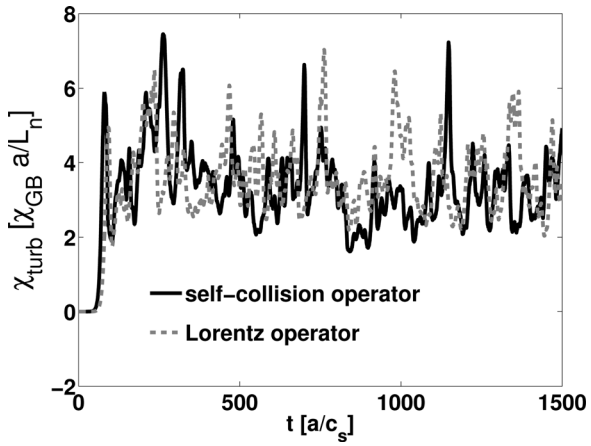

FIG. 23. For $\nu_0^* \simeq 0.14$ and $R_0/L_{T_0} = 6.9$, time evolution of the turbulent heat diffusivity χ_{turb} averaged between $r/a = 0.4$ and $r/a = 0.6$, predicted by both the Lorentz operator (grey dashed line) and the Landau self-collision operator (black plain line). The turbulent transport level in a time-average sense is accurately described by the Lorentz operator.

In order to reduce the importance of the neoclassical transport compared to the turbulent transport, the gradient $R_0/L_{T_0} = 6.9$ is then chosen, along with a weaker collisionality $\nu_0^* = 0.14$. The simulation is carried out in this latter case without any neoclassical initialization phase. Figure 23 shows the evolution in time of the turbulent heat diffusivity $\chi_{\text{turb}} = Q_{\text{turb}}/n|\nabla T|$, averaged between $r/a = 0.4$ and $r/a = 0.6$, for both operators. The difference is obviously small, at least in a time-average sense: $\langle\chi_{\text{turb,Lorentz}}\rangle_{\text{time}}/\langle\chi_{\text{turb,self-coll}}\rangle_{\text{time}} = 1.05$. The discrepancy is again probably not significant relatively to the statistical error. The Lorentz approximation for ion-ion collisions appears thus to make sense in the frame of collisional ITG turbulence simulations, at least for a moderate collisionality. However, the Lorentz approximation is obviously inappropriate for handling neoclassical transport of ions.

VII. CONCLUSION

The issue of ion-ion collision effects on electrostatic ITG turbulent transport has been studied through robust collision algorithms implemented in the global gyrokinetic code ORB5. Our turbulence simulations with collisions have been systematically started from a neoclassical equilibrium. The so-obtained neoclassical transport level thus provides a reference for evaluating the relative effects of collisions on turbulent transport. Through ORB5 simulations, the issue of the

Downloaded 12 Apr 2012 to 128.178.234.18. Redistribution subject to AIP license or copyright; see http://pop.aip.org/about/rights_and_permissions

possible interaction between neoclassical and turbulent transport physics has been addressed: strong collisional damping of turbulence-driven zonal $\vec{E} \times \vec{B}$ flows is observed, while the shearing effect from neoclassical background $\vec{E} \times \vec{B}$ flows remains weak for the smooth density and temperature background profiles considered. As a result, a general increase in ion heat transport due to collisions is observed in agreement with previous studies within the frame of the adiabatic electron model.[13] The sources of the mentioned increased transport (neoclassical contributions and amplified turbulent contributions via interactions between collisions and zonal flows) have been emphasized and studied for different ion temperature gradients R_0/L_{T_i}.

Conditions similar to Ref. 13 have been revisited in this paper. A more extensive scan in collisionality ν^* and ion temperature gradient R_0/L_{T_i} in particular enabled to provide a more detailed characterisation of the Dimits shift softening by collisions. The width of the temperature gradient profile is varied as well in this paper. In most respects, results of Ref. 13 are confirmed: (i) Above the Dimits shift region, the synergetic effect of collisions on turbulence leads to an increased collisional turbulent transport with respect to the collisionless situation $[\chi_H^{\mathrm{tot}}(\nu^*) > \chi_H^{\mathrm{turb}}(\nu^* = 0) + \chi_H^{\mathrm{neo}}(\nu^*)]$. (ii) Within the Dimits shift region, finite turbulent transport is established through collisions (Dimits shift softening). (iii) The bursting behaviour described in Ref. 13 for ion temperature gradients in the Dimits shift region is reproduced in the case of *narrow* temperature gradient profiles, enabling a coherent regime. However, for *wider* gradient profiles a steadier regime is observed, which we have interpreted as resulting from interactions between different radial regions of the basic bursting mechanism, happening at different phases at different radii.

Both within and above the Dimits shift region for wide gradient profiles, a relatively steady state of zonal flows and associated shearing rate $\omega_{E\times B}$ is thus observed. Noteworthy is the fact that the shearing rate level at finite collisionality ($\nu^* > 0$) is only slightly reduced compared to the collisionless situation ($\nu^* = 0$). Moreover, this collisional shearing rate level appears to be only weakly dependent on the finite collisionality considered. Above the Dimits shift region, a detailed study has shown that the shearing rate level is limited by Kelvin-Helmoltz type tertiary instabilities affecting the zonal flows. It has also been shown that the instability threshold level is only weakly dependent on the collisionality. At finite ν^*, the collisional damping of zonal flows, however, requires increased drive from turbulence to reach this threshold, resulting in increased turbulent transport levels. Within the Dimits shift region, zonal flow shearing rates below the tertiary instability threshold are sufficiently strong to fully quench the turbulence (less strongly driven than for gradients above the Dimits shift region) in the collisionless regime. With finite collisionality, the average shearing rates are maintained close to the collisionless levels thanks to a finite turbulence drive counter-acting the collisional damping, thus leading to finite transport. While increasing collisionality, a balance is thus apparently maintained between strengthened zonal flow damping and additional zonal flows from amplified turbulence levels.

The tool for controlling the numerical noise in collisional turbulent simulations with ORB5, the coarse-graining procedure,[10,11] has been presented and its essential role in enabling to carry out turbulence simulations over multiple collision times, without affecting the essential physical dynamics, was demonstrated.

Finally, for both neoclassical and turbulence simulations, the Lorentz approximation for self-collisions was tested against the linearized Landau self-collision operator in ORB5, which accounts for energy diffusion and ensures the local conservation of density, parallel momentum, and kinetic energy. While a physically accurate self-collision operator is required in order to predict correctly the neoclassical transport, the Lorentz approximation is sufficient for capturing the essential features of the collisional turbulent transport in the ITG regime. However, the Lorentz approximation is inappropriate for handling properly the ion neoclassical transport and thus leads to inaccurate estimates of the total transport.

ACKNOWLEDGMENTS

Simulations were performed on the Monte Rosa CRAY XT-5 supercomputer of the Swiss National Supercomputing Center, the HPC-FF cluster of the Jülich Forschungszentrum, and the BlueGene/P supercomputer of the CADMOS project. This work was partly supported by the Swiss National Science Foundation. Two of the authors (T.V. and S.B.) would like to thank Per Helander and Clemente Angioni for useful discussions related to neoclassical transport and collision operators.

[1]Z. Lin, T. S. Hahm, W. W. Lee, W. M. Tang, and R. B. White, Science **281**, 1835 (1998).
[2]R. E. Waltz, R. L. Dewar, and X. Garbet, Phys. Plasmas **5**, 1784 (1998).
[3]P. H. Diamond, S.-I. Itoh, K. Itoh, and T. S. Hahm, Plasma Phys. Controlled Fusion **47**, R35 (2005).
[4]X. Garbet, Y. Idomura, L. Villard, and T. H. Watanabe, Nucl. Fusion **50**, 043002 (2010).
[5]F. L. Hinton and M. N. Rosenbluth, Plasma Phys. Controlled Fusion **41**, A653 (1999).
[6]T. M. Tran, K. Appert, M. Fivaz, G. Jost, J. Vaclavik, and L. Villard, in *Theory of Fusion Plasmas, International Workshop* (Editrice Compositori, Società Italiana di Fisica, Bologna, 1999), p. 45.
[7]S. Jolliet, A. Bottino, P. Angelino, R. Hatzky, T. M. Tran, B. F. McMillan, O. Sauter, K. Appert, Y. Idomura, and L. Villard, Comput. Phys. Commun. **177**, 409 (2007).
[8]B. F. McMillan, S. Jolliet, T. M. Tran, L. Villard, A. Bottino, and P. Angelino, Phys. Plasmas **15**, 052308 (2008).
[9]S. Brunner, E. Valeo, and J. A. Krommes, Phys. Plasmas **6**, 4504 (1999).
[10]Y. Chen and S. E. Parker, Phys. Plasmas **14**, 082301 (2007).
[11]T. Vernay, S. Brunner, L. Villard, B. F. McMillan, S. Jolliet, T. M. Tran, A. Bottino, and J. P. Graves, Phys Plasmas **17**, 122301 (2010).
[12]J. Candy and R. E. Waltz, J. Comput. Phys. **186**, 545 (2003).
[13]Z. Lin, T. S. Hahm, W. W. Lee, W. M. Tang, and P. H. Diamond, Phys. Rev. Lett. **83**, 3645 (1999).
[14]G. Dif-Pradalier, V. Grandgirard, Y. Sarazin, X. Garbet, and Ph. Ghendrih, Phys. Rev. Lett. **103**, 065002 (2009).
[15]Y. Idomura, H. Urano, N. Aiba, and S. Tokuda, Nucl. Fusion **49**, 065029 (2009).
[16]R. E. Waltz, J. Candy, F. L. Hinton, C. Estrada-Mila, and J. E. Kinsey, Nucl. Fusion **45**, 741 (2005).
[17]P. Ricci, B. N. Rogers, and W. Dorland, Phys. Rev. Lett. **97**, 245001 (2006).
[18]B. N. Rogers, W. Dorland, and M. Kotschenreuther, Phys. Rev. Lett. **85**, 5336 (2000).

Downloaded 12 Apr 2012 to 128.178.234.18. Redistribution subject to AIP license or copyright; see http://pop.aip.org/about/rights_and_permissions

[19]D. R. Mikkelsen and W. Dorland, Phys. Rev. Lett. **101**, 135003 (2008).
[20]Z. Lin, W. M. Tang, and W. W. Lee, Phys. Plasmas **2**, 2975 (1995).
[21]T. S. Hahm, Phys. Fluids **31**, 2670 (1988).
[22]P. Angelino, A. Bottino, R. Hatzky, S. Jolliet, O. Sauter, T. M. Tran, and L. Villard, Phys. Plasmas **13**, 052304 (2006).
[23]B. F. McMillan, P. Hill, A. Bottino, S. Jolliet, T. Vernay, and L. Villard, Phys. Plasmas **18**, 112503 (2011).
[24]S. J. Allfrey and R. Hatzky, Comput. Phys. Commun. **154**, 98 (2003).
[25]S. Satake, R. Kanno, and H. Sugama, Plasma Fusion Res. **3**, S1062 (2008).
[26]B. F. McMillan, S. Jolliet, A. Bottino, P. Angelino, T. M. Tran, and L. Villard, Comput. Phys. Commun. **181**, 715 (2010).
[27]P. Helander, Plasma Phys. Controlled Fusion **37**, 57 (1995).
[28]X. Lapillonne, S. Brunner, T. Dannert, S. Jolliet, A. Marinoni, L. Villard, T. Görler, F. Jenko, and F. Merz, Phys. Plasmas **16**, 032308 (2009).
[29]A. M. Dimits, G. Bateman, M. A. Beer, B. I. Cohen, W. Dorland, G. W. Hammett, C. Kim, J. E. Kinsey, M. Kotschenreuther, A. H. Kritz, L. L. Lao, J. Mandrekas, W. M. Nevins, S. E. Parker, A. J. Redd, D. E. Shumaker, R. Sydora, and J. Weiland, Phys. Plasmas **7**, 969 (2000).
[30]S. Jolliet, Ph. D. dissertation (Ecole Polytechnique Fédérale de Lausanne, 2009).
[31]T. Görler, X. Lapillonne, S. Brunner, T. Dannert, F. Jenko, F. Merz, and D. Told, J. Comput. Phys. **230**, 7053 (2011).
[32]M. N. Rosenbluth and F. L. Hinton, Phys. Rev. Lett. **80**, 724 (1998).
[33]C. S. Chang and F. L. Hinton, Phys. Fluids **25**, 1493 (1982).
[34]A. M. Dimits and B. I. Cohen, Phys. Rev. E **49**, 709 (1994).
[35]T. S. Hahm, Phys. Plasmas **1**, 2940 (1994).
[36]P. Helander and D. J. Sigmar, *Collisional Transport in Magnetized Plasmas* (Cambridge University Press, 2002).

Downloaded 12 Apr 2012 to 128.178.234.18. Redistribution subject to AIP license or copyright; see http://pop.aip.org/about/rights_and_permissions